Icarus 429 (2025) 116458

Contents lists available at ScienceDirect

Icarus

journal homepage: www.elsevier.com/locate/icarus

Constraining volcanic vent parameters to understand the 2007 brightness surge in Io's Tvashtar plume: A DSMC approach

A.O. Adeloye [a,*], L.M. Trafton [b], D.B. Goldstein [a], P.L. Varghese [a], A. Mahieux [a,c,d]

[a] Department of Aerospace Engineering and Engineering Mechanics, The University of Texas at Austin, Austin, TX 78712, United States
[b] Department of Astronomy, The University of Texas at Austin, Austin, TX 78712, United States
[c] Belgian Institute for Space Aeronomy, Brussels, Belgium
[d] European Space Agency (ESAC), Madrid, Spain

ARTICLE INFO

Keywords:
Tvashtar
Rarefied gas dynamics
Plumes
Io
Radiative transport

ABSTRACT

Io's Tvashtar volcanic plume displayed an irregular order of magnitude increase in brightness during the 2007 New Horizons (NH) flyby as the solar phase angle of Io relative to NH increased. High-resolution NH/LORRI images captured the Tvashtar plume's evolution throughout the flyby. We investigate potential causes for the brightness surge by examining whether changes in Tvashtar's volcanic vent properties could have explained the observed brightness increase.

Using the captured NH images, a robust method is developed to constrain some of Tvashtar's vent properties. This method involves a sensitivity study of free parameters at Tvashtar's vent using axisymmetric Direct Simulation Monte Carlo (DSMC) simulations incorporating both gas and grain radiation modeling. The analysis examines how variations in these parameters (such as vent stagnation temperature, area, mass flow rate, and grain mass loading) influence the plume canopy's height, width, and overall shape.

The sensitivity analysis identifies the vent stagnation temperature and area as the parameters most influential on the plume's canopy characteristics. Given the visibility of Tvashtar's plume canopy throughout the NH flyby, canopy spatial coordinates are extracted from each LORRI image. Subsequently, a Levenberg-Marquardt optimization algorithm is employed to fit DSMC simulation plume canopies, parameterized over a two-dimensional space of stagnation temperature and area, to each extracted canopy. This process yields the optimal pair of vent stagnation temperature and area that best models the observed plume canopy for each case.

From the fitting process, we hypothesize an asymmetric source region at Tvashtar, consistent with previous research findings. However, the fitting process also determines that the observed increase in brightness cannot be entirely attributed to changes in vent conditions during the flyby, as there appears to be no correlation between these changes and the surge in brightness. The most plausible explanation for the brightness surge lies in the optical scattering properties of the plume particulates.

1. Introduction

The Jovian moon Io is the most volcanically active body in the Solar System, with hundreds of active volcanoes. A large SO_2 plume was initially detected at Pele during the Voyager flybys (Morabito et al., 1979). Since Voyager 1, multiple flybys of Io and the Jovian system have occurred. These missions yielded observations of Io's dynamic atmosphere and intense volcanic activity.

McEwen and Soderblom (1983) distinguished the volcanic plumes on Io into two main classes: (1) Pele-type plumes which are larger, producing canopies that reach as high as ~370 km above Io's surface with deposition ring diameters of ~1300 km, and (2) Prometheus-type plumes which are smaller, producing canopies that reach as high as ~80 km with deposition ring diameters of ~300 km.

Galileo's Solid-State Imager (SSI) observed the Tvashtar Catena close to Io's north pole (centered near 62°N, 122°W) between 1999 and 2001 (Milazzo et al., 2005). Using the Solid-State Imaging (SSI) system onboard the Cassini spacecraft in December 2000, Tvashtar was discovered to produce a ~ 400 km high Pele-type plume and an annular deposit around itself (Milazzo et al., 2005). On April 17, 2006, a volcanic outburst on Io's northern hemisphere was observed using the OSIRIS imaging spectrometer at the Keck Observatory, and continued activity

* Corresponding author.
E-mail address: adeloye@utexas.edu (A.O. Adeloye).

https://doi.org/10.1016/j.icarus.2025.116458
Received 20 September 2024; Received in revised form 11 December 2024; Accepted 13 January 2025
Available online 16 January 2025

was confirmed on June 2, 2006 (Laver et al., 2007).

In 2007, the New Horizons (NH) spacecraft flew by the Jovian system on its way to Pluto. It revealed a Pele-type plume eruption (~350 km high) above Tvashtar Catena (Rathbun et al., 2014). Over the course of the flyby, which lasted more than three days, the Long-Range Reconnaissance Imager (LORRI) and Multispectral Visible Imaging Camera (MVIC) obtained multiple images of the volcanic eruption of Tvashtar. These images revealed a surprising and uneven tenfold increase in Tvashtar's plume brightness (Trafton et al., 2018) as the solar phase angle between the Sun, Io, and NH increased from ~30° to 150°; see Fig. 1.

This phenomenon cannot be explained without understanding how the plume material flows and how different factors within the plume influence that flow. McDoniel et al. (2019) showed that giant plumes on Io are largely unaffected by ion bombardment from Jupiter's plasma torus, as the plasma does not penetrate the relatively dense plume. This, along with Io's thin atmosphere, means there is little outside the plume source could affect gas flow and entrained particle dynamics. Therefore, any alterations in the plume's structure and characteristics are likely attributed predominantly to factors or processes within the plume itself.

Various competing mechanisms within the plume contribute to its observed structure and properties: (1) the eruption mode, (2) the rarefied gas expansion into vacuum, (3) the gas-grain two-phase flow interactions, (4) the radiative transport within the plume involving gas absorption and emission from internal energy states, (5) the grain absorption and emission over the continuous spectrum, (6) the gas-lava interactions, and finally (7) the grain-lava radiative interactions. Important input parameters to consider at the vent include (a) the stagnation temperature—temperature of the gas when it is brought adiabatically to rest, (b) mass flow rate— total mass of material (gas and grains combined) expelled from the vent per unit time, (c) area, (d) aspect ratio—the ratio of the length of the major axis to the length of the minor axis of the vent, (e) grain mass loading of particulates entrained in the gas flow (Jessup and Spencer, 2012), and (f) grain size distribution (McDoniel et al., 2015). Numerical simulations can provide valuable insight into understanding how the interplay of these parameters with flow physics affects the properties seen in the plume by NH.

The Direct Simulation Monte Carlo (DSMC) method, developed by Bird (1994), is the best available technique for modeling a wide range of continuum-to-rarified flows. Prior axisymmetric DSMC simulations of Ionian plumes by Zhang et al. (2003) included parametric studies of vent parameters to match earlier Voyager observations. McDoniel et al. (2015) constructed 3-D DSMC simulations of Pele guided by the Galileo flyby observations. They found that the vent stagnation temperature is pivotal in determining the plume canopy height. Hoey et al. (2021) also conducted parametric studies using 3-D DSMC to investigate the impact of aspect ratio on the plume canopy height in the case of Tvashtar. They found that a 3 × 1 vent aspect ratio reasonably replicates the width of Tvashtar's plume in a few of the LORRI images.

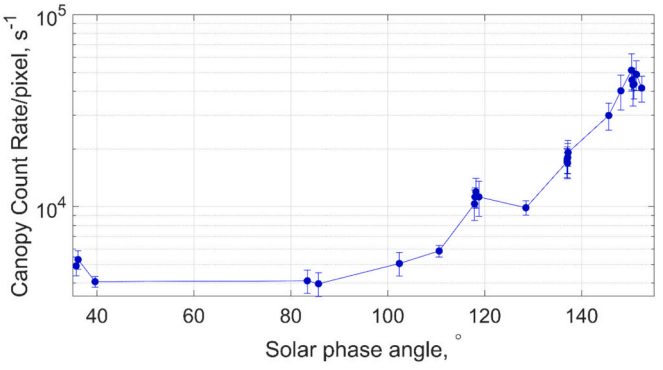

Fig. 1. LORRI Tvashtar canopy count rate per pixel as a function of NH solar phase angle. The count rate per pixel and its error bar are derived from LORRI deconvolved counts in the brightest region of Tvashtar's canopy in each image. The mean and standard deviation of pixel counts within a 25 km radius are calculated and then divided by the camera exposure time, yielding the canopy count rate per pixel and its associated uncertainty (reproduced from Trafton et al., 2018).

The notable brightness surge in Tvashtar's canopy may stem from a range of factors, including significant alterations in volcanic activity during the flyby. This could include an increase in the mass flow rate output from the vent, fluctuations in the width or narrowness of the vent's lava area, shifts in lava temperature, or condensation within the plume canopy. Additionally, variations in grain sizes throughout the flyby—where larger grains might be brighter due to enhanced light scattering—or dependence of the particle cross-section on the scattering phase angle could contribute to the variable brightness phenomenon.

When active, Tvashtar's caldera may display the venting characteristics of a hot lava lake or fire fountain (McEwen et al., 1998; Howell et al., 2001; Milazzo et al., 2005). During the NH flyby, the lava lake process is more likely, given the cosine-like variation in Tvashtar's hotspot power output with emission angle (Rathbun et al., 2014).

This work aims to characterize the unexpected brightness increase of Tvashtar's plume during the flyby and identify its underlying causes, specifically by examining whether changes in volcanic activity, driven by alterations in vent parameters, can fully explain the observed phenomenon. We present a robust method, validated with NH observational data, to constrain vent parameters in Ionian Pele-type plumes by measuring their physical dimensions. This approach uses DSMC simulations to study the sensitivity of plume dimensions to Tvashtar's vent parameters, followed by a Levenberg-Marquardt (LM) fitting process to match simulated particulate fields to LORRI observations. The method effectively constrains vent parameters while providing uncertainties and assessing their relationship to the observed brightness changes during the flyby.

A limitation of our methodology is the exclusion of modeling physical processes such as condensation, sublimation, and potential episodic particle injection at Tvashtar's vent, which are beyond the scope of this work but could influence the observed plume characteristics. For example, NH LORRI images rarely show a continuous, upgoing column of particles from the vent to the canopy (central spout), suggesting that a significant fraction of visible plume particles may be condensates rather than non-volatile particles directly emitted from the vent (Spencer et al., 2007). Ackley et al. (2021) modeled traveling waves in the plume and demonstrated that condensation and sublimation could influence grain size evolution. They also proposed that the absence of a central spout might be explained by episodic particle ejection from narrow fissures, analogous to Strombolian eruptions on Earth.

In our simulations, particle ejection is modeled as continuous, and the analysis assumes steady-state plumes, resulting in a prominent central spout in our DSMC plume profiles. While these simplifications are necessary for computational feasibility, they highlight the need for future studies to explore transient and non-equilibrium processes to fully understand the dynamics of Tvashtar's plume.

2. Methodology and results

Our in-house DSMC code, PLANET, simulates representative numerical molecules through movement and collisions to capture plume physics. The PLANET code, developed in-house and written in the C programming language, is a robust tool designed to simulate complex physical phenomena. It has the capability to model high-speed molecular and ion collisions, chemical reactions, two-phase flow dynamics, droplet formation, and radiation processes. This versatility allows for comprehensive analysis of plume behaviors and interactions under varying conditions. PLANET also models grains as particles that can be fully coupled with the gas, particularly in flow regimes where the density and collision rates are sufficiently high to sustain such coupling. In regions where the flow enters the Knudsen regime and gas-grain

interactions become less frequent, PLANET accounts for the reduced viscous and thermal coupling between the grains and the gas. Previous versions of PLANET, combined with spacecraft data, were used to simulate Pele (Zhang et al., 2003, 2004; McDoniel et al., 2015, 2017, 2019), Tvashtar (Hoey et al., 2016, 2021; Ackley et al., 2021), and Prometheus plumes (Zhang et al., 2003, 2004). This work builds on those studies by incorporating a grain radiation model in a two-phase flow with two-way coupling between gas and grains (Burt and Boyd, 2004) and enhancing the gas opacity model introduced by Zhang et al. (2003).

Molecules and grains are sourced from a "virtual vent" approximately 1 km above Io's surface, where the actual vent likely features bubbling lava. Below this virtual vent, extensive multi-phase mixing, influenced by shock and expansion waves, results in a uniform flow around the 1 km altitude (McDoniel et al., 2015). The virtual vent's placement corresponds to the altitude where this mixed medium converges into a uniform flow. The conditions below the virtual vent, including gas exit Mach number, temperature, and velocity, were previously modeled by McDoniel et al. (2015) for Pele-type plumes and are adopted here to reduce computational costs, avoiding the significant expense of modeling the flow from the lava surface to 1 km.

During the flyby period, both high-resolution LORRI and, to a lesser extent, lower-resolution MVIC images captured many structures within Tvashtar's plume. These structures arise from the complex features of the vent. The LORRI bandpass is panchromatic, covering 350–850 nm, while MVIC samples 400–975 nm at several broadband filter wavelengths (Blue, Red, NIR, and CH_4). Only the high-resolution LORRI images have been deconvolved and subsampled 2:1 (Hoey et al., 2021; Ackley et al., 2021). Therefore, we use the LORRI observations to constrain the plume simulations, which have a resolution of 1 arcsec/pixel vs. 4.1 arcsec/pixel for MVIC.

While PLANET can replicate many observed features and aid in understanding their origin and evolution, as demonstrated by McDoniel et al. (2015) for Pele, it faces a significant limitation: NH's images, taken from over 2 million km away, lack the resolution needed to accurately capture detailed vent geometry. Although the Galileo images offer high-resolution views of the Tvashtar region, the shift from an active fire fountain to a lava lake (Rathbun et al., 2014) suggests that the surface geometry has likely changed, making the NH images unsuitable for constraining vent geometry during the NH flyby. Consequently, the simulation is limited to basic vent shapes, which restricts the ability to reproduce complex 3-D effects visible in some flyby images. Nevertheless, this simplified approach enables a clearer understanding of how basic vent geometries and flow physics influence plume characteristics such as height, width, and aspect ratio.

Previous DSMC simulations of Tvashtar by Hoey et al. (2021) and Ackley et al. (2021) used rectangular vents with various aspect ratios. In this work, we use circular vents to model the lava lake volcano at Tvashtar (Rathbun et al., 2014) and simulate axisymmetric flows with improved physical models, later assessing the impact of the vent aspect ratio on the results. This method minimizes computational expense while still achieving a satisfactory alignment with LORRI images.

We conduct a sensitivity study to evaluate how different vent parameters influence plume processes and affect plume dimensions and shape. The parameters examined include stagnation temperature, mass flow rate, area, grain mass loading, and grain size distribution. Pele-type plumes are highly sensitive to vent stagnation temperature and area, with moderate sensitivity to mass flow rate and grain mass loading. Using NH line-of-sight grain column density computations, canopy extractions, and polynomial fittings via the LM algorithm, we fit LORRI images to determine optimal vent parameters. Comparing these parameters against the solar phase angle could reveal correlations that explain flyby observations.

2.1. Tvashtar vent input and boundary conditions

The Tvashtar plume transitions from highly collisional conditions near the vent to a nearly free molecular regime about 100 km above the surface, then becomes collisional again as the canopy forms a shock structure at ~300 km altitude. To model the entire plume, we simulate it under axisymmetric conditions in four physical stages within a 1°-slice from a circular vent (see Fig. 2). These stages are one-way coupled, allowing particles to move only from a lower to an upper stage due to their supersonic velocities, ensuring they do not return once they cross boundaries. Since we only consider the results at steady state, each stage has its own time step, chosen to resolve the mean collision time between the species in that stage. Exiting particle information is stored in some files for the next stage. Table 1 outlines the domain parameters for each stage, similar to those in the plumes of Hoey et al. (2021). Also, each stage uses different cell decompositions to resolve flow characteristics like mean free path, shock waves, expansions, and collisions across the varying flow regimes in the plume.

Computational gas molecules and grains are generated from a "virtual" vent, following the approach by McDoniel et al. (2015). These gas molecules are assigned velocities and temperatures corresponding to Mach 3 conditions. For instance, at a vent where the lava (and thus the gas stagnation) temperature is 1280 K (Rathbun et al., 2014), SO_2 gas molecules at the virtual vent, positioned approximately 1 km above the surface, are given a mean velocity of 895 m/s and a temperature of 515 K.

In the simulations, the grains are modeled as following log-normal size distributions as log-normal distributions have been used in prior studies (McDoniel et al., 2015) to model particle sizes in Pele's plume and they have been shown to produce deposition patterns consistent with observational data. We adopt the log-normal grain-diameter distributions (Eq. (1), adapted from McDoniel et al., 2015) and velocities fit from McDoniel et al. (2015) for Pele. From these log-normal distributions, we select nine discrete size bins (see Table 2) and a characteristic grain diameter (see Fig. 3) that can effectively capture the physics of that size range. The number of discrete-size bins is chosen to accommodate the computation time, which increases with the number of bins and the precision of the calculations.

$$f_1(d) = \frac{d^3}{N_1}\left[\frac{\alpha}{\sigma_1\sqrt{2\pi}d}exp\left(-\frac{(log(d)-\mu_1)^2}{2\sigma_1^2}\right)+\frac{\beta}{\sigma_2\sqrt{2\pi}d}exp\left(-\frac{(log(d)-\mu_2)^2}{2{\sigma_2}^2}\right)\right] \tag{1a}$$

$$f_2(d) = \frac{d^3}{N_2}\left[\frac{1}{\sigma\sqrt{2\pi}d}exp\left(-\frac{(log(d)-\mu)^2}{2\sigma^2}\right)\right] \tag{1b}$$

In Eq. (1), d represents the particle diameter in nanometers, N_1 and N_2 are a normalization factors ensuring that the total probability density described by $f_1(d)$ and $f_2(d)$ sums to 1 over the entire range of d from 20 to 10,000 nm. Eq. (1a) describes the bimodal log-normal distribution,

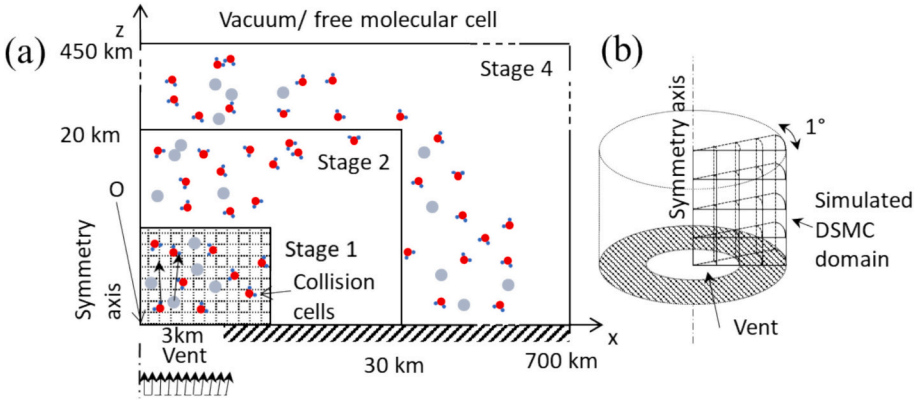

Fig. 2. (a) Schematic of panels illustrating stages and setup of the axisymmetric DSMC simulations. (b) Depiction of the simulated 1°-slice domain. Adapted from Mahieux et al. (2019).

Table 1
The simulation and domain parameters for each stage of a full calculation.

Stage	1	2	3	4
Time-step [s]	0.025	0.1	0.25	0.5
Total Time [s]	30	150	450	3750
Domain Radius [km]	6	30	100	700
Domain Height [km]	6	20	50	450

Table 2
Grain mass fractions for each size class bin of the total grain mass in the plume, derived from the log-normal distributions in Eq. (1) and simulated using the DSMC method. The fractions are normalized, summing to a total of 1.

Grain size classes, d_1-d_2 [nm]	Mass fraction (unimodal) $\sum_{d=d_1}^{d_2} f_1(d)$	Mass fraction (bimodal) $\sum_{d=d_1}^{d_2} f_2(d)$
20–120	0.0036	0.0051
120–320	0.0123	0.0184
320–520	0.0153	0.0065
520–720	0.0169	0.0021
720–1000	0.0273	0.0016
1000–2500	0.1507	0.0363
2500–5000	0.2628	0.2223
5000–7500	0.2599	0.3437
7500–10,000	0.2512	0.3640

which is the sum of two log-normal distributions. In this equation, α is 0.6422, μ_1 is 4.25 nm, σ_1 is 0.623 nm, β is 5.939×10^{-4}, μ_2 is 7.75 nm, and σ_2 is 0.797 nm. Conversely, Eq. (1b) represents the unimodal log-normal distribution, characterized by a single log-normal distribution where μ is 7.51 nm, and σ is 2.81 nm. The standard deviation-to-mean ratio is approximately 38 % for the bimodal distribution and about 54 % for the unimodal distribution. According to Murray et al. (2012), modeling the continuous grain size distribution with 3 to 4 discrete grain diameters is appropriate. This discrete binning simplification helps streamline the computational aspects of our DSMC simulations.

McDoniel et al. (2015) demonstrated that both unimodal and bimodal distributions provided reasonable fits for dust size distributions, but the bimodal distribution was more effective at capturing the complexities of particle generation within the plume. The unimodal distribution struggled to account for a gap around 1 μm in the size distribution, which suggests the presence of distinct particle generation mechanisms. In contrast, the bimodal distribution effectively represents the dual processes involved in particle formation by fitting two log-normal distributions—one with a smaller mean size and the other with a larger mean size. This approach accounts for both small particles generated through mechanisms such as filament formation and larger particles produced by explosive spattering.

Furthermore, McDoniel et al. (2015) found that the mean size based on number density derived from the bimodal distribution (approximately 88 nm) closely aligns with observations reported by Jessup and Spencer (2012), reinforcing its validity. This suggests that the true size distribution of dust particles in the plume is best represented by a combination of two log-normal distributions, indicating the involvement of two different particle creation mechanisms.

To assess the sensitivity of Tvashtar's plume canopy height and width to the grain size distribution under nominal vent conditions (as shown in Table 4), we simulated two Tvashtar plumes—one using the bimodal distribution and the other using the unimodal distribution (the density profiles for each grain size class are detailed in Appendix A). The

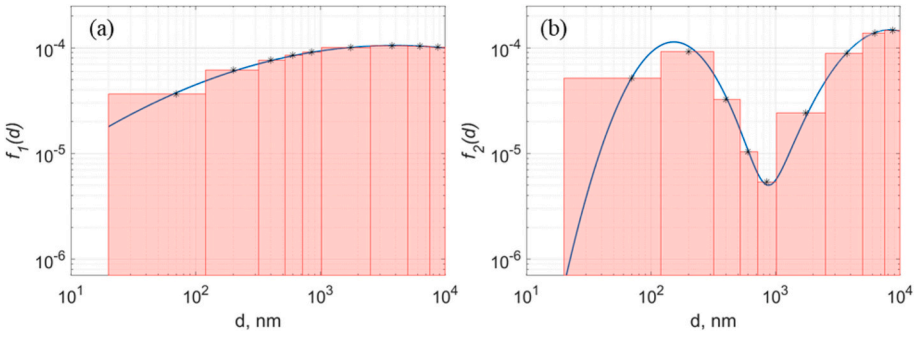

Fig. 3. This figure compares two types of grain size distributions. The blue curves represent (a) unimodal and (b) bimodal log-normal distributions of grain mass fraction as a function of grain diameter. The red histograms indicate nine distinct bins of grain sizes derived from DSMC simulations. The area of each histogram corresponds to the area under the blue curve within the respective bin margins. Black markers denote the representative diameters for each bin. (For interpretation of the references to colour in this figure legend, the reader is referred to the web version of this article.)

simulations show an average difference of 1.8 % in maximum plume height and 4.9 % in radial deposition distance for the plume gas and grain size classes. Additionally, consistent structural characteristics were observed in both simulations. However, based on the earlier findings by McDoniel et al. (2015), all subsequent plume simulations in this study utilize the bimodal distribution, as the axisymmetric plume structure appears to be independent of the grain size distribution.

2.2. Grain radiation modeling in PLANET

In our grain radiation model, mechanisms by which grains exchange radiation as gray bodies include (1) absorption of solar radiation, (2) thermal emission from Io's cool surface, (3) radiation from a localized high-temperature lava source/vent, and (4) radiation from the adjacent/enveloping hot SO_2 gas, and (5) emission of grain thermal radiation to the surroundings. Details about the grain radiation model implementation are provided in Appendix B.

2.3. Gas radiation modeling in PLANET

In this study, we use the same methods for modeling radiative cooling due to microwave and infrared radiation from the rotational and vibrational modes of SO_2 as the ones used by Zhang et al. (2003, 2004), McDoniel et al. (2015, 2017), and Hoey et al. (2016, 2021).

Zhang et al. (2004) first explored the effect of gas opacity in Ionian plumes like Pele and Prometheus, where radiation from the gas is trapped due to high densities. Hoey et al. (2021) expanded this study to Tvashtar, finding that gas opacity contributed to higher plume canopy heights and wider deposition rings. The opacity model divides the plume into two regions: an opaque region with high gas densities, where radiation is quickly/locally reabsorbed, and a transparent region, where radiation escapes to space without reabsorption. In this model, excited molecules can only radiate to lower vibrational levels in the transparent spectral regions; in opaque portions of the plume radiative loss is not permitted.

Building on this approach, we now use an improved opacity model to better represent radiative energy from the gas's vibrational bands (Table 3), especially in the plume's densest regions near the vent. The wavenumbers and Einstein-A coefficients for each ro-vibrational band, shown in Table 3, are calculated by taking a weighted average over all lines within the band, where the weights are based on the respective line intensities or Einstein-A coefficients. Instead of using a single-line absorption coefficient, as done previously by Zhang et al. (2004) and Hoey et al. (2021), we compute a band absorption coefficient from all lines in each of the three SO_2 vibrational bands. This modification more accurately captures the band strength and opacity surfaces. We also introduce a threshold band coefficient in the DSMC simulation to determine whether molecules in each cell can emit or reabsorb radiation. Additional details on constructing the band absorption coefficient are provided in Appendix C.

Our updated opacity model in PLANET corrects the earlier version's reliance on a single central line within a vibrational band, which led to excessive energy confinement in the plume, beyond what is indeed achievable.

In a standard scenario with nominal vent conditions (see Table 4), the new opacity model reveals that the ν_1 stretching mode (~1153 cm^{-1}) and ν_2 bending mode (~521 cm^{-1}) are transparent throughout the plume; see Fig. 4b. This means that excited SO_2 molecules can immediately cool by radiating to space from these modes, with the cooling rate increasing for modes with higher Einstein-A coefficients. In contrast, the ν_3 stretching mode (~1360 cm^{-1}) shows an opaque region extending ~18 km above the vent's center, differing from the earlier Zhang et al. (2004) model, where all three vibrational modes had opaque regions under the same vent conditions (Fig. 4a).

Table 3
Relevant rovibrational bands for SO_2 (Gordon et al., 2022).

Rovibrational Band	Wavenumber (cm^{-1})	Einstein-A Coefficient (s^{-1})
ν_1 (Fundamental)	1153	1.04
ν_2 (Fundamental)	521	0.28
ν_3 (Fundamental)	1360	19.19

Table 4
Sensitivity Study Free Parameters and definition of the Nominal case.

			Nominal		
Stagnation Temperature, T_o [K]	1080	1180	**1280**	1380	1480
Mass flow Rate, $\dot{m}$ [kg/s]	50,000	66,667	**100,000**	150,000	200,000
Grain mass loading, f_g [%]	0	2.5	**5**	7.5	10
Area, A [km^2]	5	15	**30**	45	55

To evaluate the impact of the gas opacity and radiation models on the plume, we disable the gas opacity model but keep radiative cooling from rotational and vibrational states active (Fig. 5b). Here, excited molecules can de-excite regardless of the surrounding flow field properties, like temperature and density. For comparison, in Fig. 5c, we deactivate all gas radiation models within the plume. This prevents molecules from radiative cooling via vibrational or rotational modes and leaves collisions as the only cooling mechanism.

As the gas ascends from the vent in the nominal plume, a temperature drop occurs (discussed later in Section 3.1). Temperatures near the vent for the nominal plume are slightly higher (Fig. 5a) than in the scenario where gas opacity is deactivated (Fig. 5b). In Fig. 5c, where all gas radiation mechanisms are turned off, the temperature beneath the first expansion wave remains uniform, consistent with expectations for a Mach 3 gas dynamic expansion unaffected by radiative effects. Fig. 6 shows that the plume with all gas radiation models deactivated has the tallest and widest canopy, while the nominal plume has a slightly wider canopy and a y increased height compared to the plume with the opacity model deactivated (entire plume is assumed optically thin).

The current opacity model conservatively simulates the energy confinement within the plume by preventing energy loss through band radiation in any opaque cell or region—representing one extreme case. At the other extreme, with opacity disabled, radiative cooling from vibrational bands occurs regardless of opacity. In reality, some energy escape likely happens from an opaque cell or region. Fig. 6 shows that both extreme cases produce plumes with nearly identical gas canopy heights and widths. While our implementation is basic in the sense that it could be enhanced by using a more expensive photon Monte Carlo technique coupled with DSMC, as demonstrated by Prem et al. (2019), for modeling radiative transport from an expanding H_2O cloud, the current opacity model yields results within acceptable error margins (<1 % influence on the height and width of the plume). Thus, we incorporate this model into all plumes presented in this work.

2.4. Nominal plume

2.4.1. Near-vent flow

We examine the flow properties near the vent in our nominal plume to understand how energy evolves within the plume and how different physical mechanisms modeled in the DSMC calculation compete and influence this evolution as the plume rises. Fig. 7 displays gas number density contours near the vent as the flow expands into the vacuum. An expansion wave, characterized by the supersonic flow diverging from the central axis, results in gradual decreases in flow properties such as density, pressure, and temperature while the flow speed increases. The first clear expansion wave originates from the edge of the ~3 km vent and reaches the symmetry axis at around 10 km altitude.

In a simple isentropic gas flow, properties like density, temperature, and velocity would remain constant below the first expansion fan.

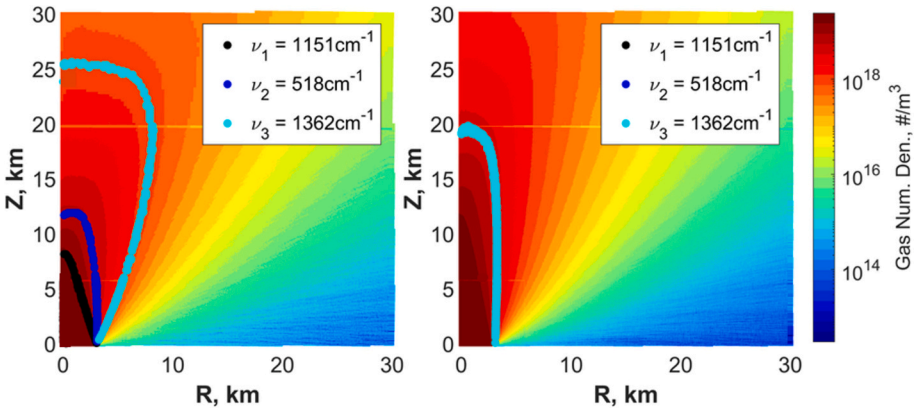

Fig. 4. (a) Opacity surfaces derived using the gas opacity model of Zhang et al. (2004). (b) Opacity surfaces in the improved opacity model. The background is the gas number density in the near-vent region of the plume.

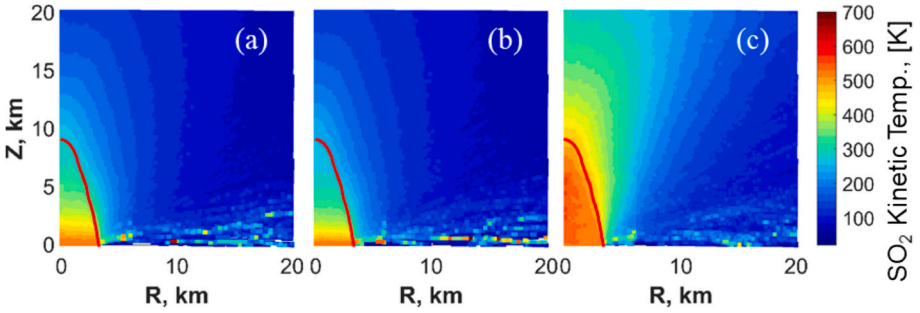

Fig. 5. Kinetic temperature profiles for gas-only plumes in the vicinity of the vent under three conditions: (a) nominal plume with all models active, (b) deactivation of the gas opacity model, and (c) deactivation of all gas radiation mechanisms. The red line shows the first expansion wave originating from the edge of the virtual vent. (For interpretation of the references to colour in this figure legend, the reader is referred to the web version of this article.)

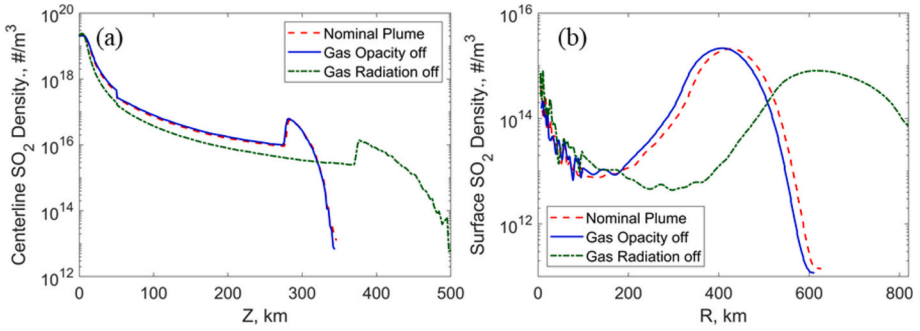

Fig. 6. Number density profiles along the symmetry axis for SO_2 gas plotted against altitude (a) and radial distance from the vent along Io's surface (b). The profiles are shown for three plumes: one with all gas radiation models deactivated, one with the nominal opacity model active, and one with only the opacity model deactivated. This comparison illustrates the effects of different gas radiation treatments on plume characteristics.

However, our model is more complex due to factors such as grains entrained in the gas flow, radiation absorbed and emitted by gas and grains, and the coupling of gas internal energy modes with the radiation field. Each effect varies in magnitude and characteristic time scale. As shown in Fig. 7a, the gas density remains nearly constant, but the kinetic temperature (Fig. 7b) decreases as molecules exit the vent, dropping by nearly 250 K by the time they reach the first expansion wave. This drop is due to microwave and infrared radiation from the rotational and vibrational modes, which leads to a decrease in rotational temperature. The gas kinetic temperature follows this trend, decreasing alongside the rotational temperature due to the high intermolecular collision rate (~4000 collisions/molecule/s), which keeps these modes nearly in equilibrium.

Fig. 8a-c illustrates that the gas vibrational temperature quickly diverges from local thermodynamic equilibrium once the collision rates begin to decline, occurring as the gas passes the first expansion wave, indicated by the black line. Fig. 8d further illustrates the mean energy expressed as an equivalent temperature of the energy modes of SO_2 as a function of altitude near the vent. The optically thin ν_1 and ν_2 modes decay through radiation, while intermolecular collisions maintain equilibrium with the opaque ν_3, rotational, and translational modes until the flow crosses the opacity surface at ~14 km. At this point, the ν_3 temperature rapidly declines to zero, induced by its high Einstein-A coefficient, followed by a sharp drop in the ν_1 temperature at ~15 km. Fluctuations in ν_1 and ν_3 temperatures at higher altitudes result from statistical noise typical of DSMC simulations. The ν_2 temperature decays steadily at a slower rate, reflecting its lower Einstein-A coefficient, while rotational and translational temperatures stay in equilibrium longer,

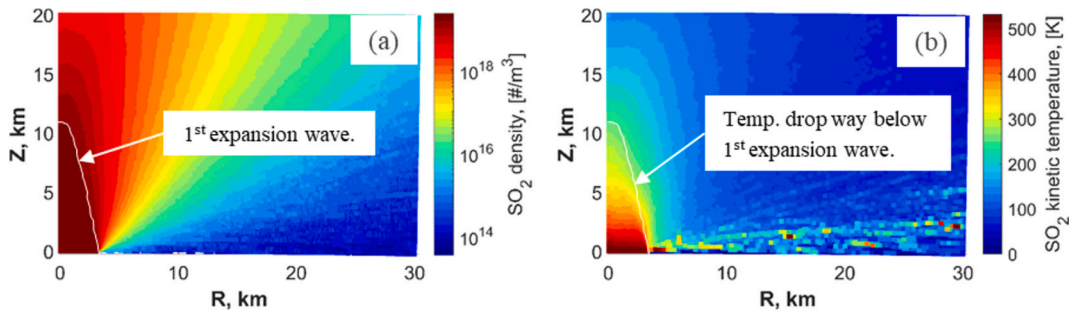

Fig. 7. (a) Near vent SO_2 number density map. (b) Near vent SO_2 kinetic temperature map. The white line is the first expansion wave from the virtual vent edge to the symmetry axis.

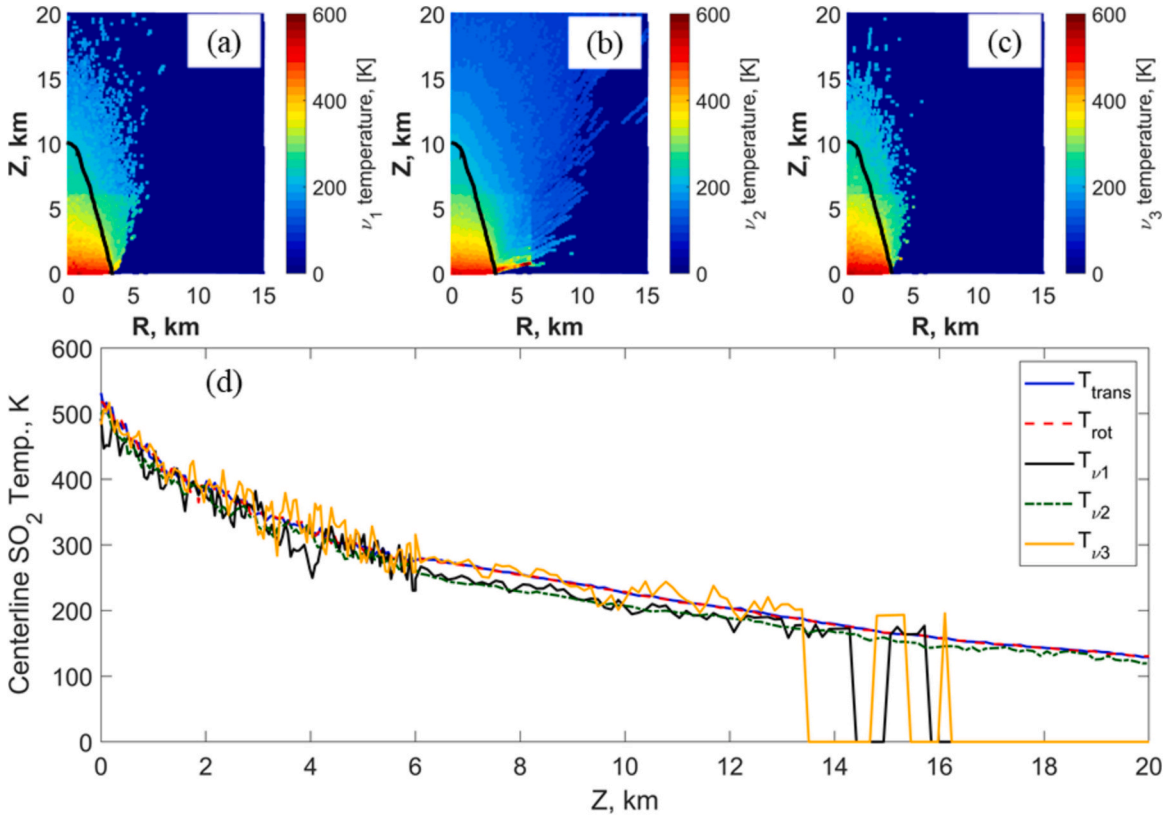

Fig. 8. Contour plots of band temperature for the three vibrational modes of SO_2 in the vent's vicinity (a) ν_1 band, (b) ν_2 band, (c) ν_3 band. (d) Translational and internal temperatures of SO_2 along the symmetry axis as a function of the altitude in the vent's vicinity. The black line in panels a-c is 1st expansion wave from the virtual vent edge to the symmetry axis.

only deviating at higher altitudes where reduced collisions prevent equilibrium.

Gas-grain collisions cause grains to disperse, with the extent of horizontal spreading depending on their size—smaller grains spread more widely than larger ones. About 20 km above the vent, the smallest grains (the 20–120 nm bin) spread approximately 17 km radially (Fig. 9). In contrast, the 0.72–1.00 μm grains spread around 9 km, and larger 7.5–10.0 μm grains disperse only 5 km at the same altitude.

Fig. 9 also shows a temperature decline for the 20–120 nm grains as the distance from the vent increases, a trend that becomes more pronounced at altitudes much greater than the vent radius. A similar temperature variation is observed across the other grain sizes in the simulation.

2.4.2. Overall plume species profiles

Fig. 10 displays the full plume number density contours for both gas and discrete grain sizes under nominal conditions. The gas reaches a peak altitude of ~350 km at steady state, with a canopy shock altitude of ~277 km and a radial deposition distance of ~600 km on Io's surface. When examining the aggregate grain umbrella profiles of all size classes, the maximum altitude reaches ~318 km, while the maximum deposition distance extends to around 499 km.

The derived deposition ring is smaller than observed around Tvashtar during the Galileo flyby era, when the average radius of the ring was approximately 720 km (Geissler et al., 2004). This finding aligns with the fact that the Galileo flyby measured active lava flow over an area of 6.3 km^2 (Milazzo et al., 2005). In contrast, during the New Horizons flyby, the active lava flow spanned 30 km^2 (Rathbun et al., 2014). As discussed in Section 3.2, this increase in vent area is associated with a negative correlation to the plume deposition width.

Some grains fall back through the gas canopy, colliding with ascending gas molecules to form distinct inner shock-like grain

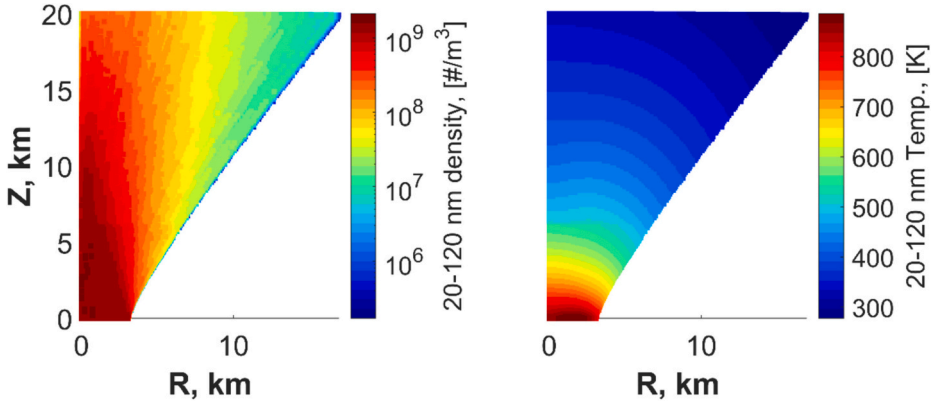

Fig. 9. Contours of (a) number density and (b) temperature for 20–120 nm grains for the nominal vent and boundary conditions.

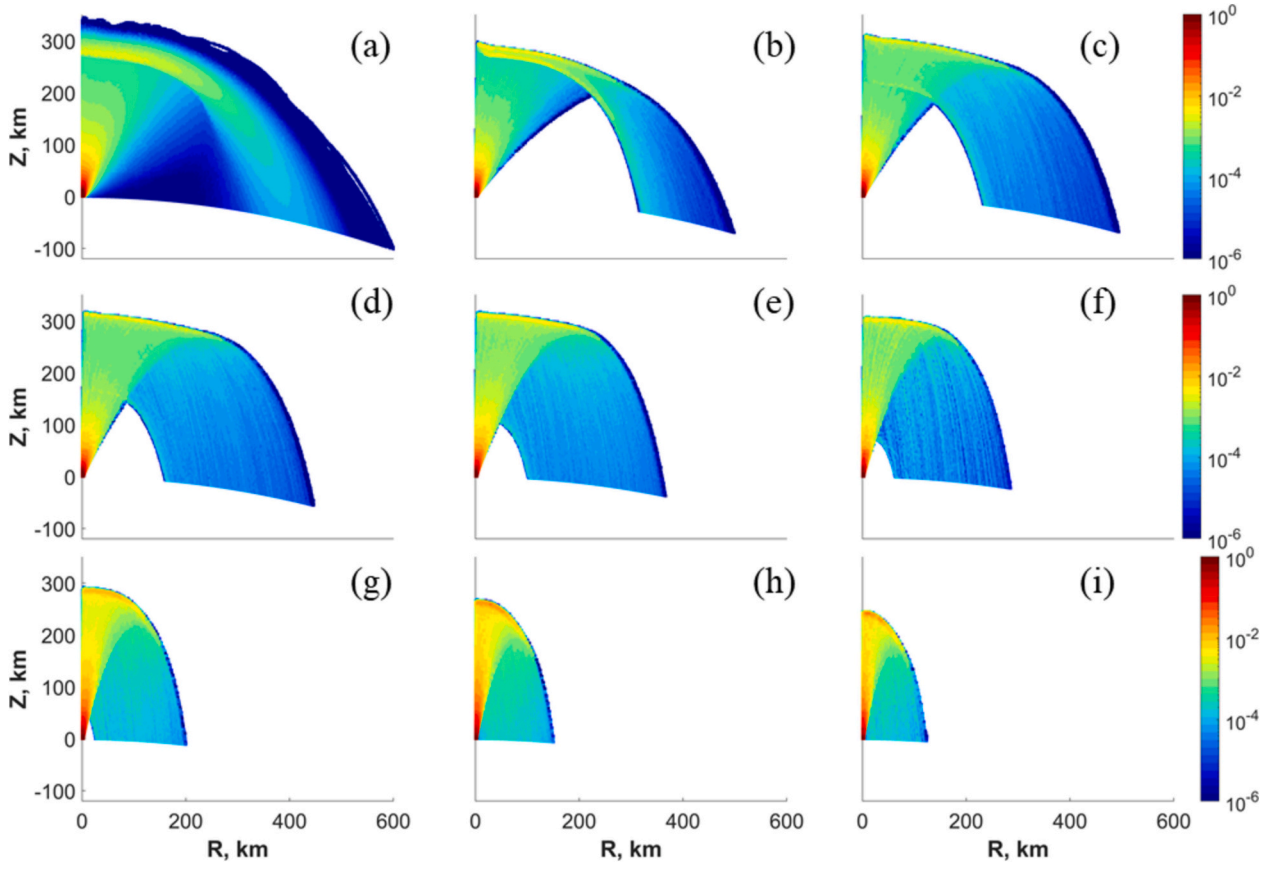

Fig. 10. Number density profiles for gas and eight out of nine-grain sizes in the simulation normalized by the vent number density of that class. (a) SO_2 gas; (b) 20–120 nm grains; (c) 120–320 nm grains; (d) 320–520 nm grains; (e) 0.72–1.00 μm grains; (f) 1.00–2.50 μm grains; (g) 2.50–5.00 μm grains; (h) 5.00–7.50 μm nm grains; (i) 7.5–10.0 μm grains.

umbrellas. These inner umbrellas form due to gas-grain collisions whereby ascending gas molecules counteract the vertical momentum of falling grains, causing grains to disperse horizontally. As grain size increases, the altitude of the second umbrella decreases. Additionally, contours reveal that grains larger than 2.5 μm lack an inner umbrella due to insufficient rising gas momentum to suspend them.

The dense layer of slow-moving gas molecules above the gas dynamic canopy shock hinders the motion of both ascending and descending grains, shaping their trajectories and forming the outer umbrella profile for grains with enough momentum to reach that altitude. Similar phenomena were reported by Zhang (2004).

2.5. Sensitivity study

We carry out a sensitivity study to assess the impact of changing the plume's input boundary conditions on the canopy height and width. Table 4 describes the vent parameters that are varied around a nominal set.

Each parameter is varied independently, with all other parameters held at their nominal values (as listed in Table 4). This approach results in 17 simulations, allowing us to assess the influence of individual parameters without the substantial computational cost associated with exploring every possible permutation, which would involve running 625 simulations. The heights and widths of the gas canopy and grain

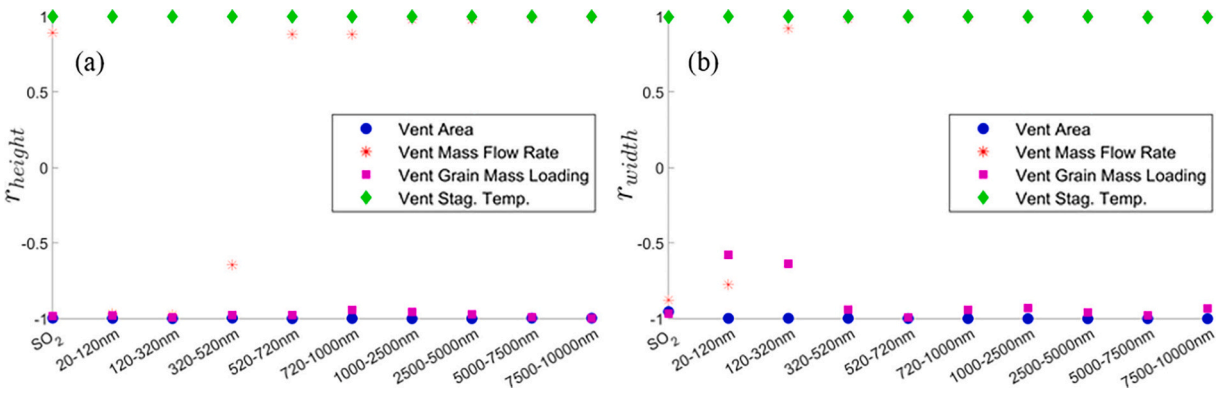

Fig. 11. Correlation coefficients for the changes in gas and each of the nine-grain size classes with changes in canopy/umbrella dimensions (a) heights and (b) widths.

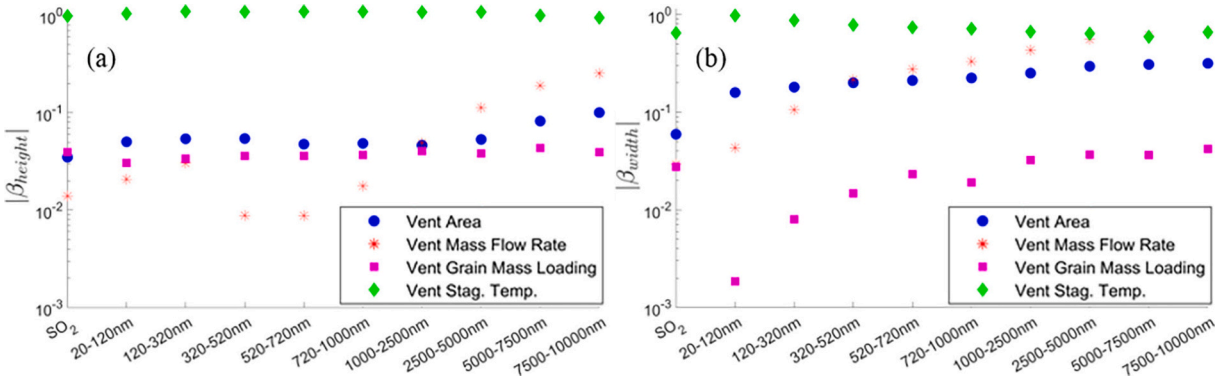

Fig. 12. Absolute elasticity for vent parameters relative to gas and individual grain size class canopy/umbrella dimensions (a) Heights and (b) Widths. Absolute elasticity quantifies the magnitude of proportional changes among the parameters, whereas the linear correlation coefficient indicates the direction of these changes (Fig. 10).

umbrellas from the sensitivity study are measured and recorded in Table D.1 (Appendix D). To assess the relationship between the parameters and the umbrellas, both linear correlations (Fig. 11) and elasticity of log-log regressions (Fig. 12) are calculated. The correlation coefficient, r, measures the strength and direction of the linear relationship between two variables, with $r = \pm 1$ indicating a perfect linear relationship and $r = 0$ indicating no correlation. Elasticity, denoted as β, is the slope of a log-log regression, capturing the proportional (percentage) change relationship between two variables. For example, $\beta = \pm 1$ indicates that a 1 % change in the independent variable results in a corresponding $\pm 1\%$ change in the dependent variable.

Fig. 11 shows how r varies for gas and grains depending on which physical processes dominate within the plume when each vent parameter is adjusted. Strong correlations ($r \approx +1$) are generally observed between umbrella heights/widths and vent stagnation temperature and mass flow rate, while strong anticorrelations ($r \approx -1$) are seen with vent area and grain mass loading.

Fig. 12 depicts that the heights and widths of the gas canopy and grain umbrellas are most sensitive to changes in vent stagnation temperature ($|\beta| \approx 1$), suggesting that umbrella shapes and curvatures remain roughly preserved as they uniformly expand or contract in response to changes in vent stagnation temperature.

The absolute height elasticity, $|\beta_{height}|$ (Fig. 12a), and width elasticity, $|\beta_{width}|$ (Fig. 12b), vary across the three remaining vent parameters, with no single parameter consistently dominating the influence on all grain umbrella dimensions. This variability likely arises from the complex interplay of physical processes and the differing sensitivities of each grain size class to these processes. Typically, umbrella widths are more sensitive to changes in vent area than umbrella heights. As a result, variations in the vent area affect the height, width, and shape/curvature of both the gas canopy and grain umbrellas.

The effect of varying grain mass loading on umbrella heights is consistent across all grain size classes and is comparable to the influence of vent area and mass flow rate (Fig. 12a). However, its impact on umbrella widths is consistently weaker than that of the other parameters (Fig. 12b).

The mass flow rate affects different grain sizes and gases in varying ways. For grains smaller than 520 nm, its influence on umbrella heights and widths is less significant compared to other factors. However, as grain size increases, the impact of mass flow rate becomes more pronounced, surpassing the effects of area and grain mass loading for grains larger than 2.5 μm and eventually exceeding the sensitivity to stagnation temperature in the largest grain size class.

2.6. Fitting DSMC simulations to LORRI observations

Our goal is to determine whether Tvashtar's volcanic activity remained stable during the NH flyby or if changes in activity contributed to the significant plume brightness increase observed by LORRI (Fig. 1). To do this, we extract the plume umbrella edge spatial coordinates from each deconvolved LORRI image and apply an LM algorithm to these coordinates, comparing them against interpolations of a series of DSMC simulations that span the vent parameters most sensitive to plume umbrella dimensions. This process yields a set of vent parameters for each LORRI image that best match the observed plume umbrella.

The sensitivity analysis (Section 2.5) showed that the plume dimensions, especially for grain classes with the largest physical dimensions (canopy height and width), are more sensitive to changes in

vent stagnation temperature and area compared to changes in vent mass flow rate or grain mass loading (Fig. 12). We generated a 5 × 5 parametric grid using the stagnation temperature and vent area values from Table 4, resulting in 25 DSMC simulations. Each simulation utilized a distinct parameter pair from the grid while maintaining the remaining vent parameters at their nominal values (Table 4).

To extract the plume umbrella edge and its spatial coordinates from each deconvolved LORRI image, we followed this procedure:

(1) Fit a circle to Io's limb using a MATLAB algorithm (Smith, 2015) and calibrate each image using the circle's radius and center coordinates in pixels.
(2) Minimize smear and artifacts by removing pixels with intensity less than 50 to 100 % of the average pixel intensity, aiding in identifying the plume umbrella boundary from Io's surface and glare.
(3) Extract the pixels marking the plume umbrella and convert their pixel coordinates to spatial coordinates relative to the fitted circle's center coordinates from Step 1. Fig. 13a and d illustrate this procedure applied to a LORRI image. This step was automated through a custom MATLAB algorithm, which facilitated an efficient and consistent execution of the procedure.

Hoey et al. (2021) deconvolved 25 LORRI images that captured irregular brightness increases and detailed the NH observing geometry for each image, including distance from Io, viewing longitude/latitude, and solar phase angle, as summarized in Table 1 of their study. Using this information, along with DSMC grain number density profiles and the fitted circle data from Step 1 of the LORRI umbrella edge extraction procedure, we compute column density images of Tvashtar from the NH perspective (see Fig. 13b for an example). For each NH observing geometry, 25 column density images map the area-stagnation temperature parameter space, as described earlier.

To determine the vent parameter pair that best fits the extracted LORRI umbrella (Fig. 13d), we extract column umbrella edges from the column density images using Step 3 of the LORRI umbrella extraction procedure (see Fig. 14 for samples). Fig. 14 illustrates the variation in the overall plume umbrella shape when altering one of the vent parameters. The vent stagnation temperature impacts the umbrella shape more uniformly, whereas changes in the vent area predominantly affect the plume width rather than its height (See Section 3.2). We use a set of high-order multivariate polynomials (detailed in Appendix E) to construct a surrogate function for each LORRI image. This function approximates the behavior of the true column umbrella function across the entire parameter space by interpolating or extrapolating between the DSMC simulation data points, allowing estimation of column umbrella properties for any parameter combination within the defined space.

The LM algorithm is then applied to identify the area-stagnation temperature pair within each surrogate function's space that best matches the observed LORRI umbrella. Various sources of error are considered, including (1) circle fitting (Step 1), (2) polynomial/surrogate function error, (3) DSMC noise, (4) plume instability, and (5) the error outputted by the LM algorithm itself. Among these, plume instability is the most significant error source. Its impact on the results of the LM algorithm is assessed using an 8-min period during the NH flyby, where a sequence of 5 snapshots taken on March 1, 2007, which revealed dynamic changes in the plume's shape due to multiple waves within the canopy (Hoey et al., 2021; Spencer et al., 2007). The remaining vent parameters do not contribute to the error analysis since their values are kept constant.

Given the brief time between successive movie frames, it is unlikely that any changes in vent stagnation temperature or area would significantly alter the umbrella's structure. Therefore, vent conditions are assumed to remain stable throughout the 8-min duration. However, the LM algorithm shows fluctuations in stagnation temperature and area across these 5 movie frames (Fig. 15a). The average LM-derived vent parameters are 1176 K and 6.8 km^2, with standard deviations (SD) of 38 K and 2.6 km^2, respectively. Notably, a strong correlation of 0.84 is observed among these five epochs. These deviations are considered absolute model errors due to umbrella instability, and they are assumed applicable to all other epochs as well.

Since the remaining LORRI images were captured at much longer intervals ranging from hours to days, it is impossible to assess minute-scale umbrella instability using single images. Therefore, the umbrella instability error from the movie frames is extended to the LM fitting error across all 25 images, assuming consistent instability throughout the flyby. Thus, the total error is represented as the square root of the sum of the squares of two independent errors: (1) the intrinsic error produced by the LM algorithm during parameter fitting and (2) the error associated with umbrella instability, which reflects temporal variations in the plume structure.

The analysis reveals an average vent stagnation temperature of 1266 K (SD = 92 K) and a vent area of 20 km^2 (SD = 13 km^2) based on the 25 images examined. These findings are consistent with those of Rathbun et al. (2014), who reported colour temperatures of 1240 ± 60 K (Red/NIR ratio) and 1280 ± 100 K (Red/CH4 ratio) from observations taken by the MVIC camera aboard NH. Their study further indicated that a temperature of 1280 K corresponded to a flow size of 30 km^2, while

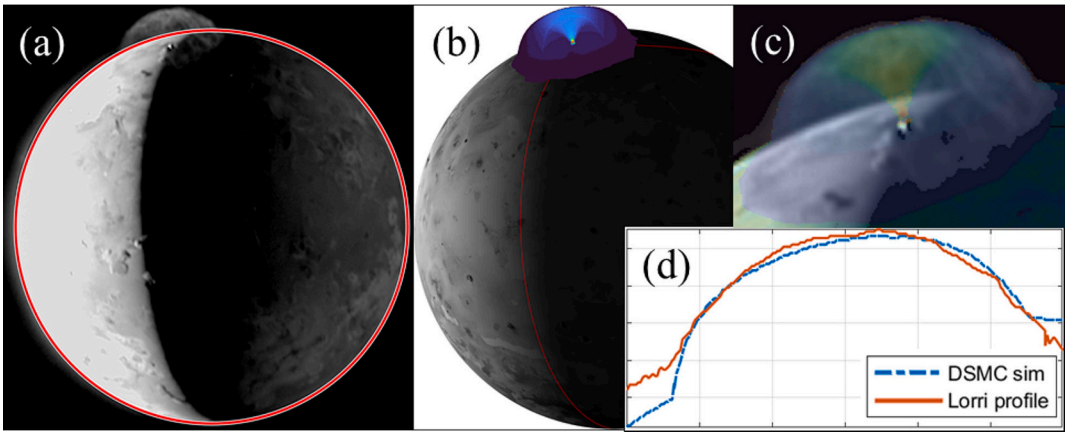

Fig. 13. (a) LORRI image taken on 28-Feb-2007 at 15:15:24 UTC, with a fitted red circle outlining Io's limb. (b) Associated column density image using nominal DSMC vent parameters, both images sharing the same pixel density. (c) Zoomed-in overlay of LORRI and column density images, showing the alignment of vent locations. (d) Extracted plume canopy (umbrella edges) from LORRI and column density images, where the blue dashed line is the DSMC simulation result, and the red line is the LORRI umbrella. (For interpretation of the references to colour in this figure legend, the reader is referred to the web version of this article.)

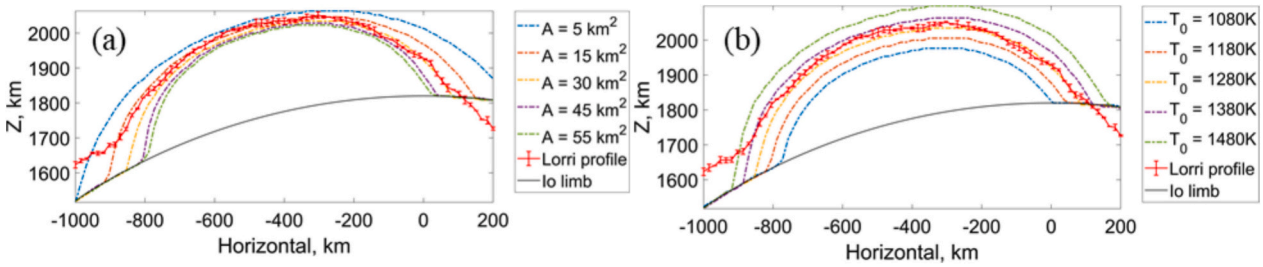

Fig. 14. Extracted column density profiles corresponding to the plume as shown in Fig. 13. (a) Set of five plume column density edges from DSMC simulations with varying vent areas while holding the stagnation temperature constant at 1280 K. (b) Set of five plume column density edges from DSMC simulations with varying stagnation temperatures while maintaining a constant vent area of 30 km^2. The complete set of these extracted column umbrellas is provided to the LM algorithm, which identifies the parameter pair that best matches the extracted LORRI umbrella (also shown).

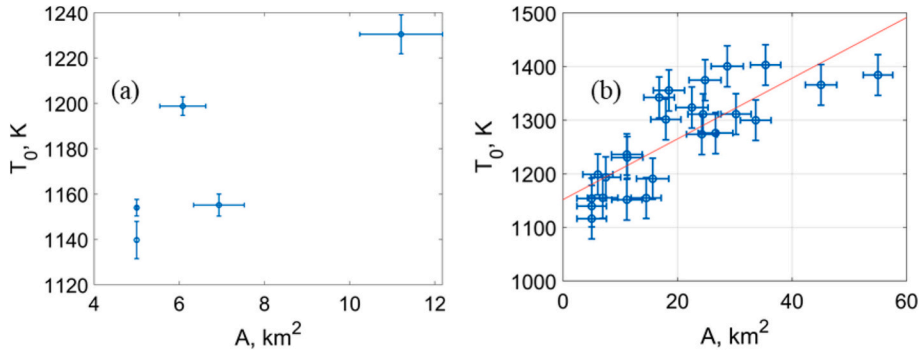

Fig. 15. (a) Relationship between vent area and stagnation temperature for the 5 movie frames. Error bars are the combined uncertainties from the least-square fitting, polynomial fitting, and circle fitting procedures. (b) Relationship between vent area and stagnation temperature derived from LM algorithm optimization for all 25 LORRI observations. Error bars are the cumulative uncertainties from all examined error sources around each observation. Note the correlation between the area and stagnation temperature.

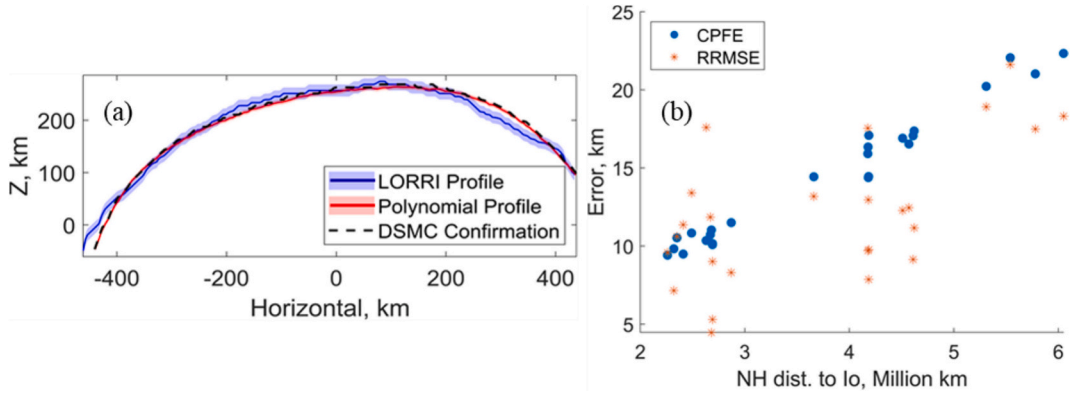

Fig. 16. (a) Comparison of example umbrellas from the LORRI image captured on 28-Feb-2007 at 15:15:24 UTC, highlighting agreement between the polynomial profile and DSMC profile for the best-fit vent parameters. (b) Analysis of the RRMSE and CPFE with the NH distance from Io (x-axis). The errors show similar magnitudes, confirming our method.

1240 K was associated with a flow size of 50 km^2. Additionally, the results agree with Tsang et al. (2014), who determined that the Tvashtar hotspot had a temperature of 1239 ± 19 K and an area of 37 (+4/− 3) km^2. These consistent findings bolster the credibility of the current analysis. Additionally, a strong correlation of 0.80 is found between these parameters (Fig. 15b).

To validate our method and results, we run best-fit DSMC simulations based on optimized vent parameters, generate corresponding column density images, and extract column umbrellas.

We compare these umbrellas with those generated by polynomial functions and the actual LORRI observations (see Fig. 16). The residual root mean square error (RRMSE) for the polynomial-generated umbrellas closely matches the combined errors from the circle fitting and polynomial fitting procedures (CPFE). For a detailed explanation of these error calculations, we refer to Appendix E. Essentially, the best-fit vent parameters result in umbrella structures with uncertainties within

the expected error range, demonstrating the strong internal consistency of our method and ensuring reliable results within the acknowledged limitations.

3. Discussion

3.1. Nominal plume physics

PLANET simulates the dynamic interactions among various physical mechanisms within the plume. Near the vent (Fig. 7), gas density is primarily influenced by gas dynamic expansion, resulting in constant density and velocity until molecules cross the first expansion wave from the vent's edge. However, gas temperatures behave differently due to internal energy losses and exchanges driven by collisional interactions with grains, gas opacity, and the radiation of vibrational energy in the infrared. As discussed earlier (Section 2.3), as gas molecules ascend, those excited in the nearly transparent ν_1 or ν_2 bands can emit energy to space, while emission from the ν_3 band is restricted until the molecules pass through the opacity surface. In this dense plume region, collision rates are very high ($\sim 10^4$ s^{-1}), driving the flow toward local thermodynamic equilibrium. This promotes internal energy exchange from the ν_3 band to translation, molecular rotation, and the ν_1 and ν_2 vibrational modes, which can radiate to space because the gas is optically thin at their fundamental band wavelengths of 11.5 and 19 μm, respectively. As a result, energy loss continues from these transparent rotational and vibrational bands, causing the gas temperature to drop until nearly all molecules reach the ground state for all three bands.

Grain temperatures and velocities undergo two distinct processes. Collisions with gas molecules influence grain velocities and internal temperatures, with the grain/gas interaction generally in the partial "slip" regime (McDoniel et al., 2015). However, temperature changes are primarily driven by radiative exchanges, with the hot lava at the vent acting as a continuous energy source and empty space as a continuous energy sink. The temperature profile for 20–120 nm grains shows an anti-correlation between grain temperature and distance/orientation from the vent (see Fig. 9b).

3.2. Sensitivity study

The sensitivity study reveals how plume dimensions depend on free vent parameters and the impact of various physical models within the plume. It also clarifies how these modeled processes alter the flow as the parameters are adjusted.

Increasing the mass flow rate leads to an expansion of the opacity region for the ν_3 band, raising its height from ~13 km at 50,000 kg/s to ~26 km at 200,000 kg/s. This expansion, along with increased gas density and collision rates, enhances internal energy transfer (as described in Section 3.1). The resulting energy transfer into translation from the excited ν_3 band slightly increases the gas canopy height. However, the energy loss through radiation from the other vibrational bands reduces the overall impact of the enlarged opacity region on plume dimensions.

At higher mass flow rates, increased gas-grain collisions allow the expanding gas to transfer more momentum to the grains, enabling them to achieve greater umbrella heights and widths.

The vent stagnation temperature determines the initial energy distribution to gas and grains. Since it reflects the temperature of the hot lava lake, it also controls the amount of radiative energy available for transfer to the entrained grains within the plume. The sensitivity study shows that changes in stagnation temperature have the strongest influence on plume height and width.

The grain mass loading sensitivity study highlights the effects of two-way gas-grain collisional coupling on the plume. As shown in Fig. 17, the gas kinetic temperature along the symmetry axis is plotted for three plumes: one with 5 % grain loading, a gas-only plume (0 % loading), and one with 10 % grain loading. The temperature profile of the gas-only plume decreases uniformly from the vent due to expansion and radiative loss until it suddenly spikes at the gas canopy shock.

Grain-loaded plumes exhibit a different temperature pattern. Near the vent, the gas temperature initially drops as it expands, then gradually increases with altitude. It first peaks at an altitude corresponding to the 7.5–10.0 μm grain class umbrella (the lowest grain umbrella, below the gas canopy height). This is followed by a sharp decline and a second peak at the altitude of the 5.0–7.5 μm grain class umbrella (the second lowest, also below the gas canopy height). After another drop, the temperature rises again, reaching a final maximum at the gas canopy altitude. These distinct temperature spikes occur because the DSMC calculation groups a continuous grain size distribution into discrete classes, each represented by a single grain diameter to model the physics of that size class. While a truly continuous grain size distribution, similar to an actual plume, would show the same overall trend, the temperature spikes would be less pronounced and more smoothed out. The temperature increase as a function of altitude (>50 km) is due to gas-grain collisions occurring in three scenarios: fast-moving ascending gas with (1) slow-moving ascending grains, (2) relatively stationary grains in the umbrellas, and (3) descending grains.

The collisions scatter molecules in random directions, leading to an increase in gas kinetic temperature (Fig. 17), which measures the random motion of gas molecules in terms of their velocity. This scattering effectively decreases the upwards momentum of the gas, resulting in less momentum available for transfer to grains at higher altitudes downstream. Consequently, this leads to a decrease in both grain umbrella and gas canopy heights. Increasing the grain mass loading exacerbates the scattering effect, further reducing umbrellas and canopy heights, as shown in Fig. 17 (see Table D.1 in Appendix D for gas canopy and grain umbrella for different grain mass loading cases).

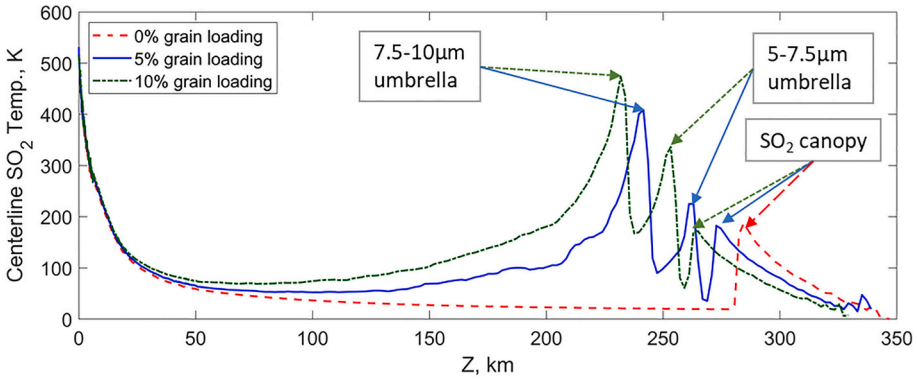

Fig. 17. Gas kinetic temperature as a function of altitude for plumes with different grain mass loading. Note: the elevated temperatures are computed in regions of non-equilibrium.

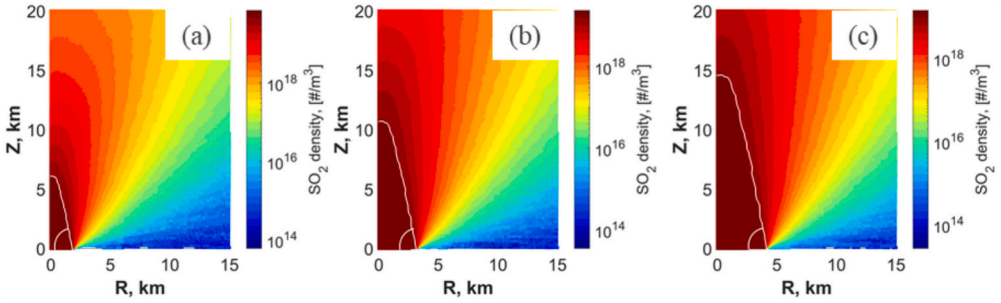

Fig. 18. Near vent number density maps for plumes with different vent area (a) 5 km^2 (b) 30 km^2 (c) 55 km^2. The white lines mark out the first expansion wave, the angle of which is approximately the same in all three cases (~75.4°).

Vent area changes impact gas rarefaction near the vent, but the expansion wave angle remains constant at the same vent Mach number. However, as vent area increases from 5 km^2 (Fig. 18a) to 55 km^2 (Fig. 18c), the expansion wave intersects the symmetry axis at higher altitudes. Significant energy loss occurs through radiation below this wave, where gas density and translational temperature drop while velocity increases. The lower density and temperature reduce energy replenishment and radiative losses. With a smaller vent radius, expansion starts lower, retaining more kinetic energy and increasing plume height and width, leading to anti-correlations between plume dimensions and vent area (Fig. 11).

3.3. Fitting DSMC simulations to LORRI observations

Combining DSMC simulations with other techniques to fit plume umbrellas in LORRI observations helps assess Tvashtar's volcanic activity during the flyby. This approach yields optimal vent area and stagnation temperature pairs, along with their uncertainties, that align with Tvashtar's plume umbrella edge at each observation (Fig. 15). However, when these values are plotted against NH's solar phase angle (Fig. 19) and compared with the observed tenfold increase in brightness, no clear trend or change in vent area or stagnation temperature explains the surge. Brightness shows a strong correlation of 0.77 with the solar phase angle, while vent area and stagnation temperature have weak correlations of -0.24 and 0.15, respectively, suggesting that changes in vent conditions alone do not account for the irregular brightness increase.

To further investigate, we explore the spatial structure of Tvashtar's vent by analyzing the relationship between the optimal (fitted) vent area and stagnation temperature values and relative longitude or longitudinal displacement of NH relative to Tvashtar during the flyby (Fig. 20). Sinusoidal functions are fitted to scatter plots of vent area (Fig. 20a: $f(x) = A\sin(Bx + C) + D$) and stagnation temperature (Fig. 20b: $g(x) = E\sin(Fx + G) + H$, where x represents the relative longitude. The parameters for these functions are as follows:

- For vent area: $A = -14.9 \pm 1.3$ km^2, $B = 2.1 \pm 0.1$, $C = 209 \pm 5°$, and $D = 24.3 \pm 0.9$ km^2. The R^2 for this fit is 0.55, and χ^2_ν is 12.06.
- For stagnation temperature: $E = -83 \pm 10$ K, $F = 2.1 \pm 0.1$, $G = -13.8 \pm 7.1°$, and $H = 1277 \pm 8$ K. The R^2 for this fit is 0.59, and χ^2_ν is 2.72.

The goodness-of-fit metrics indicate that the model captures some degree of the plume's behavior but not all processes potentially influencing it.

Regarding vent asymmetry, the sinusoidal fit of the vent area suggests there could be a directional elongation at Tvashtar's vent. This idea is consistent with previous observations, which noted the presence of complex plume structures during NH's flyby (Hoey et al., 2021). However, other unmodeled factors—like pulsing of particles out of thin cracks at the vent (Ackley et al., 2021)—could potentially influence plume width in ways that might mimic the effects of vent asymmetry. Thus, while the observed sinusoidal trend in area and the corresponding inferred vent asymmetry may suggest an elongated east-west vent, this conclusion should be regarded as a hypothesis.

From the sensitivity study, there exists a strong negative correlation between vent area and plume width. Given that vent area affects plume width more significantly than plume height (see Fig. 14a), we inferred a likely vent diameter from the optimized area. In theory, the observed umbrella width in NH images, which lies normal to the observer's line of sight, would correspond to this vent diameter. Larger observed plume widths would generally indicate a smaller optimized vent area, yielding a radius perpendicular to the observer's line of sight. From this radius, the sinusoidal trend would imply an elliptical vent shape, with the major axis oriented east-west. If valid, this orientation could align with observations of the vent's shape during earlier Galileo flybys (see Fig. 6 in Milazzo et al., 2005).

For the stagnation temperature, the fitted sine function (Fig. 20b)

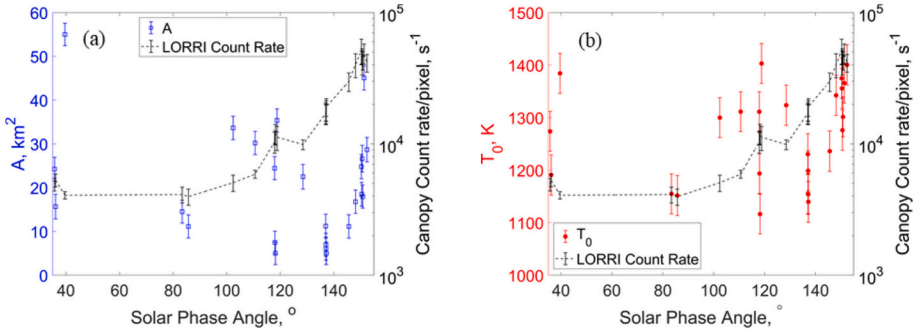

Fig. 19. Optimal vent parameters—(a) area and (b) stagnation temperature—are shown on the left y-axis as a function of Io's solar phase angle relative to NH during the flyby. The right y-axes for (a) and (b) display the brightness curve from Fig. 1, represented as canopy count rate versus solar phase angle on a logarithmic scale. Notably, the brightness curve shows a correlation of 0.77 with the solar phase angle.

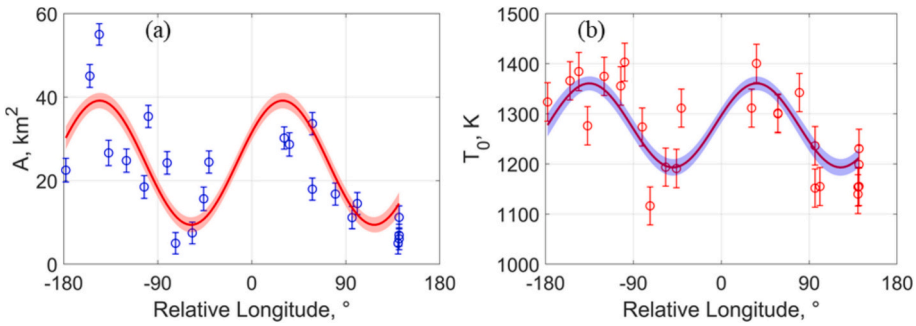

Fig. 20. Optimized vent parameters—(a) area and (b) stagnation temperature—plotted against NH's observing longitude relative to Tvashtar's longitude during the flyby. The lines represent the fitted sinusoidal functions for each parameter.

also indicates a longitudinal dependence, completing just over two cycles. However, this pattern seems less physically plausible and is more likely an artifact of the non-linear methodology, which results in a strong correlation between area and stagnation temperature (Fig. 15b).

The longitudinal dependence of the optimal stagnation temperature could be physically plausible if Tvashtar's volcanic activity exhibited episodic behavior corresponding to the observed longitudinal pattern (Fig. 20b). Volcanic vents can change over time, as seen with Tvashtar, which shifted from a fire fountain during the Galileo flybys (Milazzo et al., 2005) to a lava lake during the NH flyby (Rathbun et al., 2014). The most likely explanation, however, is an asymmetry in the lava temperature distribution (independent of area) across the lava lake, similar to models observed and predicted at the larger Loki Patera (Gregg et al., 2024). This asymmetry is not captured by the current DSMC modeling, which assumes a constant temperature across a circular lava lake. Such an asymmetric temperature distribution could result in different maximum altitudes observed by both observers, with these maxima occurring off the central axis of symmetry of the plume, as seen in some LORRI images.

4. Conclusions

This study explored the potential cause of the tenfold brightness surge observed in Tvashtar's plume during the NH flyby of Io. We examined whether changes in volcanic activity, driven by variations in vent parameters, could explain this phenomenon. Key findings include:

- A sensitivity analysis using DSMC simulations demonstrated how vent parameters (stagnation temperature, mass flow rate, vent area, and grain mass loading) impact plume morphology.
- Fitting simulated plumes to NH/LORRI observations provided optimal vent area and stagnation temperature values for each observation.
- Analysis showed no significant correlation between these optimal vent parameters and the observed brightness changes, suggesting that vent conditions alone cannot explain the brightness surge.
- Based on the analysis of the optimal vent area in relation to NH's relative longitude to Tvashtar, we hypothesize that Tvashtar's vent may be elongated with its major axis oriented east-west, a possibility that aligns with previous studies.

Future research should explore additional factors, such as variations in grain sizes which could well be driven by condensation/sublimation processes in the plume, episodic particle injection at Tvashtar's vent or the influence of particle cross-section on scattering phase angle, to better understand the 2007 brightness surge in Tvashtar's plume.

CRediT authorship contribution statement

A.O. Adeloye: Writing – review & editing, Writing – original draft, Visualization, Validation, Software, Methodology, Investigation, Formal analysis, Data curation, Conceptualization. **L.M. Trafton:** Writing – review & editing, Writing – original draft, Supervision, Project administration, Methodology, Investigation, Funding acquisition, Formal analysis, Data curation, Conceptualization. **D.B. Goldstein:** Writing – review & editing, Writing – original draft, Validation, Supervision, Project administration, Methodology, Investigation, Formal analysis, Conceptualization. **P.L. Varghese:** Writing – review & editing, Writing – original draft, Validation, Supervision, Resources, Methodology, Formal analysis, Conceptualization. **A. Mahieux:** Writing – review & editing, Writing – original draft, Supervision, Software, Methodology, Investigation, Formal analysis, Data curation, Conceptualization.

Declaration of competing interest

The authors declare that they have no known competing financial interests or personal relationships that could have appeared to influence the work reported in this paper.

Acknowledgements

This work was supported by NASA Grant 80NSSC21K0830 of the New Frontiers Data Analysis Program. We thank the Texas Advanced Computing Center (TACC) for providing computing resources.

Appendix A. Comparing 2 different grain size distributions

While various physical models compete to shape the overall plume structure, with each model's influence varying based on changes in vent parameters, changes in grain size distribution do not affect the overall plume structure. This is evident in Figs. A.1 and A.2, which display the number density profiles along the plume's centerline and across Io's surface for eight of the nine discrete grain sizes, normalized by vent number densities. The simulation results show an average difference of 1.8 % in maximum plume height and 4.9 % in radial deposition distance for both plume gas and various grain size classes. The consistent rate of change in number densities across all grain size classes, both along the centerline and on the surface, confirms that the plume's morphology remains unchanged between the two grain size distributions.

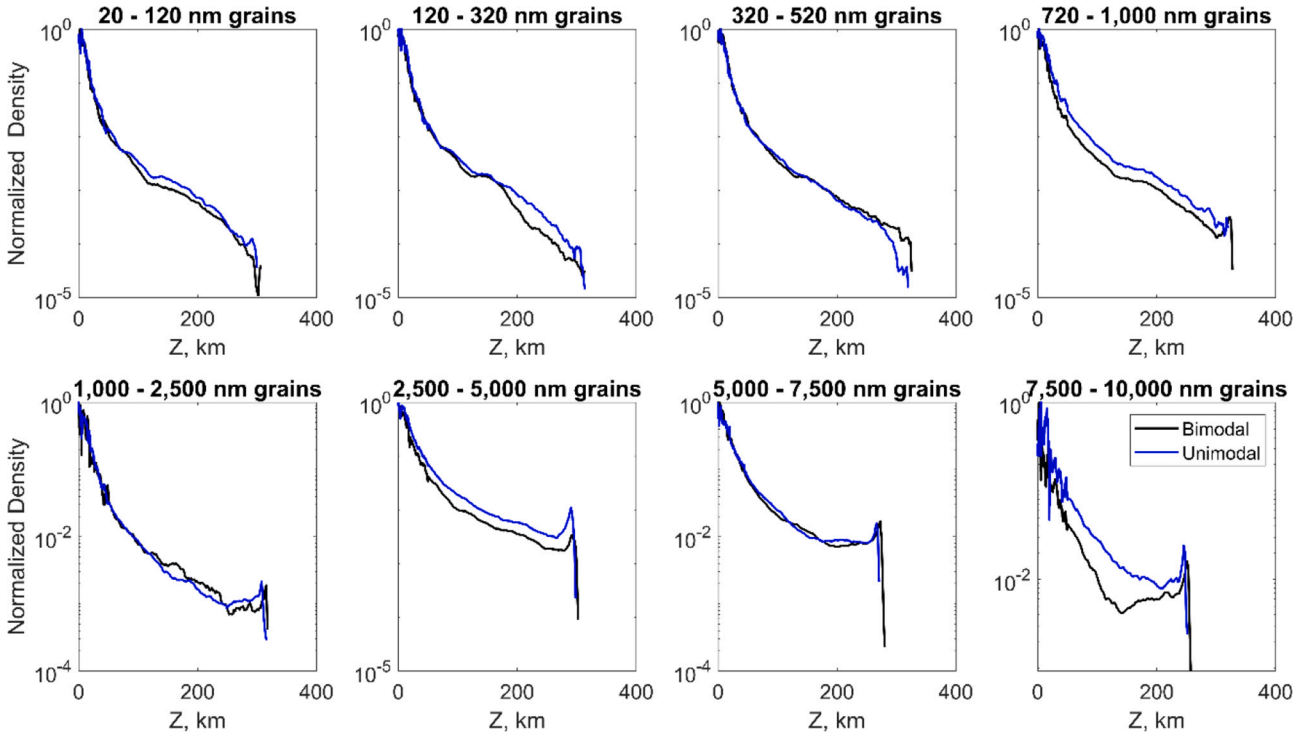

Fig. A.1. Number density profile (normalized by vent number density) along the axis of symmetry for different grain size distributions. Despite the differing mass fractions of the grains, the overall shape of the plume remains consistent for both bimodal and unimodal grain size distributions.

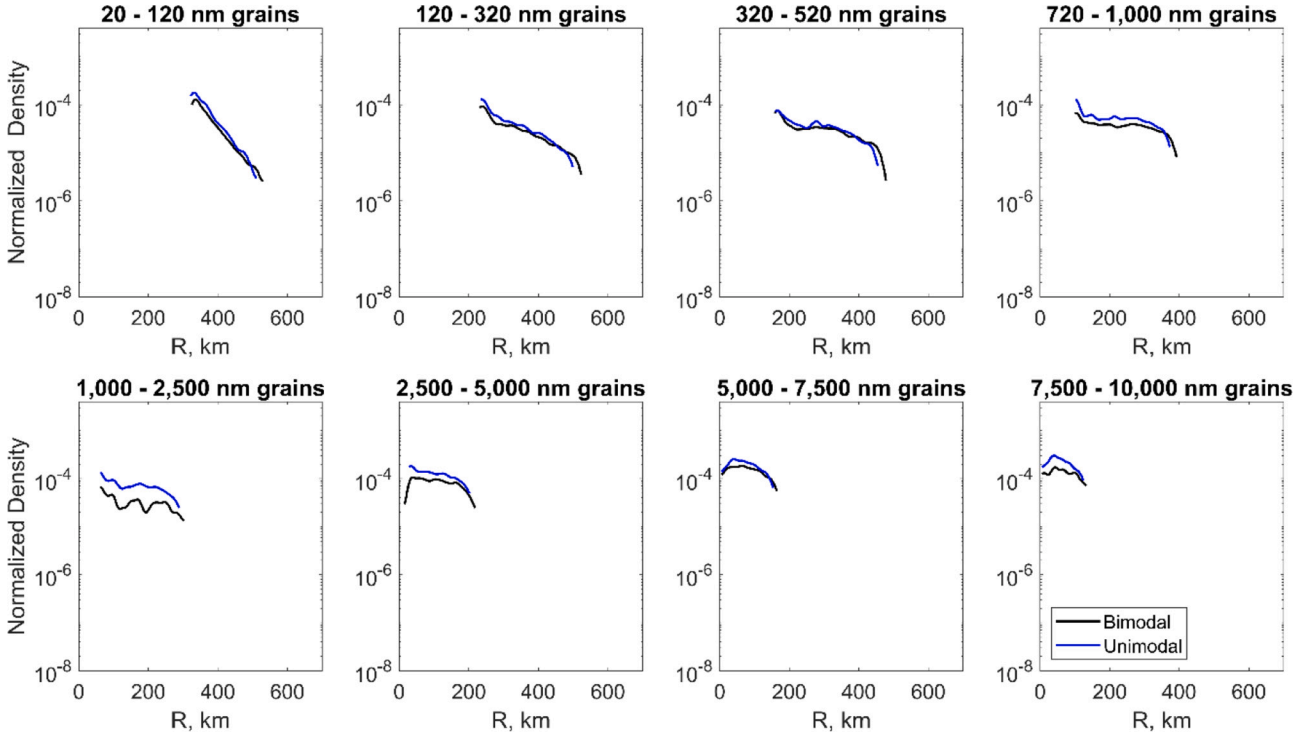

Fig. A.2. Normalized Number Density profile along Io's surface for different grain size distributions. Even though the grains have different mass fractions the overall shape of the plume is preserved for both the bimodal and unimodal grain size distributions.

Appendix B. Details of grain radiation model in PLANET

We calculate the radiative exchange between each grain and its surroundings by summing the individual contributions from different sources. First, we compute the radiative exchange between grains and the hot lava. Although our DSMC computation is axisymmetric, representing a 1° slice with a circular lava lake as the vent, we account for radiation from the entire lava surface, not just the portion within our domain (see Fig. B.1 for configuration). The circular lava vent is divided into ($N_r \times N_\theta$) discrete elements. In the simulations presented, the vent is subdivided into 51 × 51 elements, totaling 2601 elements. The thermal radiative flux from each element to the computational grains ($Q_{ij\to g}$) is calculated using Eq. (B.1a),

which involves computing the radiative exchange along the path connecting a grain to each element, based on the expression for radiative exchange between finite areas described by Howell and Siegel (1969). The overall energy flux from the lava to each grain ($Q_{l\to g}$) is then obtained by summing these individual exchanges within the domain using Eq. (B.1b).

$$Q_{ij\to g} = \frac{\epsilon_l \epsilon_g \sigma \left(T_l^4 - T_g^4\right) cos\left(\phi_{ij}\right)}{\pi \left|\overrightarrow{S}_{ij}\right|^2} \left[\int_{\theta_j}^{\theta_{j+1}} \int_{r_i}^{r_{i+1}} r' dr' d\theta'\right] \tag{B.1a}$$

$$Q_{l\to g} = \sum_{i=0}^{N_R-1} \sum_{j=0}^{N_\theta-1} Q_{ij\to g} \tag{B.1b}$$

In Eq. (B.1), $\epsilon_l \approx 0.8$ and $\epsilon_g \approx 0.8$ represent the emissivity of the basaltic lava and grain in our model (Rogic et al., 2019). T_l and T_g are the temperatures of the lava and grain, respectively. ϕ_{ij} is the angle between the normal $\hat{n}_{ij}$ to the surface of the element and the line of length $\left|\overrightarrow{S}_{ij}\right|$ connecting the grain and the element, as shown in Fig. B.1. σ denotes the Stefan-Boltzmann constant. To minimize computational costs, we pre-compute $Q_{l\to g}$ values over a fine grid covering a 50 × 50 km domain. For regions beyond this domain, where the distance between the lava and the grain increases, we simplify the calculation by treating the lava as a point source, resulting in a modified expression for $Q_{l\to g}$, as shown in Eq. (B.1c).

$$Q_{l\to g} = \frac{\epsilon_l \epsilon_g \sigma \left(T_l^4 - T_g^4\right) cos(\phi)}{\pi \left|\overrightarrow{S}\right|^2} \left[\pi R_{vent}^2\right] \tag{B.1c}$$

where ϕ is the angle between the normal at the center of the vent and the line of length $\left|\overrightarrow{S}\right|$ joining the grain to the vent. R_{vent} is the radius of the vent.

Next, we compute the radiative flux ($Q_{Sun\to g}$) from the Sun to the grains (see Eq. (B.1d)). $S_{Sun\to g}$ is the distance between the grains and the Sun (~5.2 AU), R_{Sun} is the radius of the Sun (696,000 km) and T_{Sun} is the Sun's surface temperature (5772 K).

$$Q_{Sun\to g} = \frac{\epsilon_g \sigma T_{Sun}^4}{\pi S_{Sun\to g}^2} \left[\pi R_{Sun}^2\right] \tag{B.1d}$$

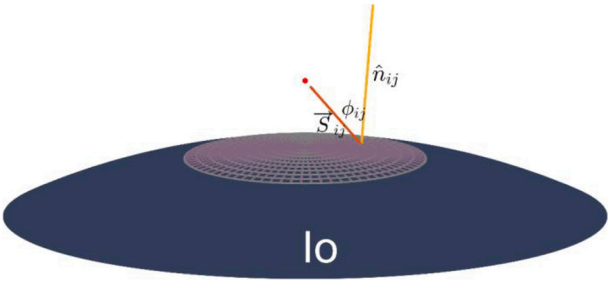

Fig. B.1. Radiative interchange between a vent element and a single lofted computational grain.

For a Pele-type plume with a canopy height of ~350 km, its entrained grains can experience microwave radiation from Io's cool surface up to ~1200 km from the center of the vent. We use a similar approach as in Eq. (A.1a) and (A.1b) for a wider circle ~1200 km in diameter and compute heat flux at every point above the surface for a domain spanning 400 × 800 km.

The final exchange is between a grain and the empty space, which can be calculated as in Eq. (B.2):

$$m_g c_p \frac{dT_g}{dt} = \left(Q_{l\to g} + Q_{s\to g} + Q_{surf\to g} - 4\epsilon_g \sigma T_g^4\right) \pi R_g^2 \tag{B.2}$$

In Eq. (B.2), m_g represents the mass of the grain, c_p is the grain's specific heat capacity of the (1170 J/(kg•K)), and R_g is the grain radius. To calculate the temperature change for each grain, we use a first-order Euler method to solve Eq. (B.2). The initial grain temperature is set based on radiative equilibrium with the lava at the vent, considering an approximate 1 km distance between the grains and the vent center.

The choice of a first-order Euler method is particularly suitable in this context due to the predictable nature of the temperature profile, which depends on the distance from the heat source. This predictability allows us to achieve satisfactory accuracy with a simpler method while minimizing computational demands.

To assess radiative heat transfer effects on the grains, the spectral radiance of lava at Tvashtar's vent is calculated as a function of altitude along the plume's axis of symmetry (Fig. B.2). Variations in lava spectral radiance are caused by grain extinction (scattering and absorption) and gas absorption. Grains cause significant attenuation—around 27 % at 10 km and 59 % at 350 km—while gas attenuation is minimal (1.33 % at 300 km), occurring only within vibrational-rotational bands. Grain extinction is determined using Mie theory (Mätzler, 2002) with the complex refractive index of basalt (Pollack et al., 1973), analyzed for 1280 K lava emitting gray body radiation. Gas absorption is calculated using the SO_2 absorption spectrum at 298 K from HITRAN (Gordon et al., 2022).

As a result, gas attenuation is negligible and does not affect the transfer of thermal radiation from lava to grains. To assess the impact of grain attenuation on energy transport, a single grain is launched vertically from the vent's center, and its internal temperature is tracked with altitude (Fig. B.3a) under various scenarios: (1) only lava radiation, (2) both lava and solar radiation, (3) no radiation sources, (4) lava radiation with grain

attenuation, and (5) both lava and solar radiation with grain attenuation. Grain attenuation is estimated from Fig. B.2.

Considering Tvashtar's location on Io, scenario (5) most accurately reflects actual conditions, as the plume is visible due to sunlight scattering throughout the flyby. Modeling this would require detailed 3-D asymmetric DSMC simulations, which are computationally intensive. However, as shown in Fig. B.3a, radiative heat transfer solely from lava radiation, unaffected by grain attenuation (Scenario 1), produces a grain temperature profile within acceptable error margins. Therefore, we select this scenario for the DSMC simulation.

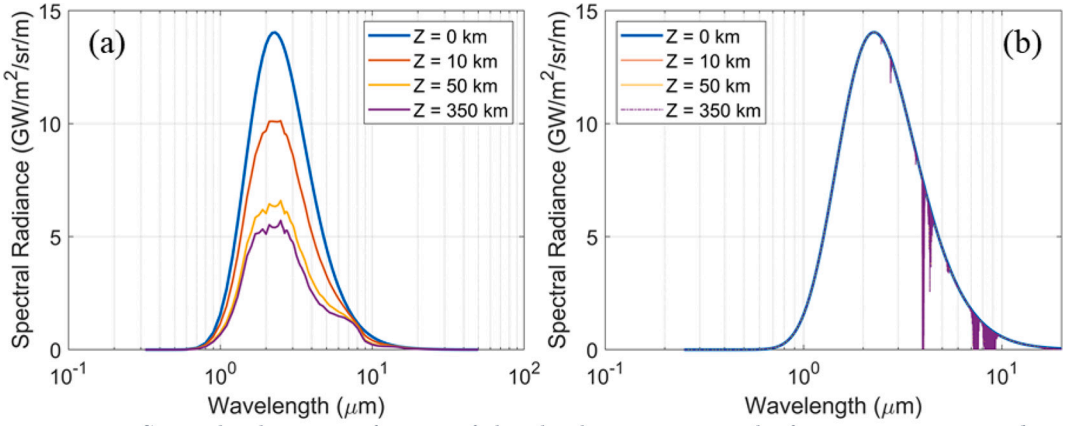

Fig. B.2. Lava Spectral radiance as a function of altitude, changing as a result of (a) grain attenuation (b) gas attenuation.

Photon mean free paths for wavelengths between 0.3 and 50 μm have been calculated for all grain size classes in the simulation, using the maximum number density for each class (Fig. B.3b). The long mean free paths, generally over 50 km, indicate that radiation emitted or scattered by grains within the plume is likely to pass through without interacting, such as through reabsorption or multiple scattering. Consequently, the grain radiation model is designed so that grains do not engage in direct radiative energy transfer with each other, nor do they interact with gas molecules through this process.

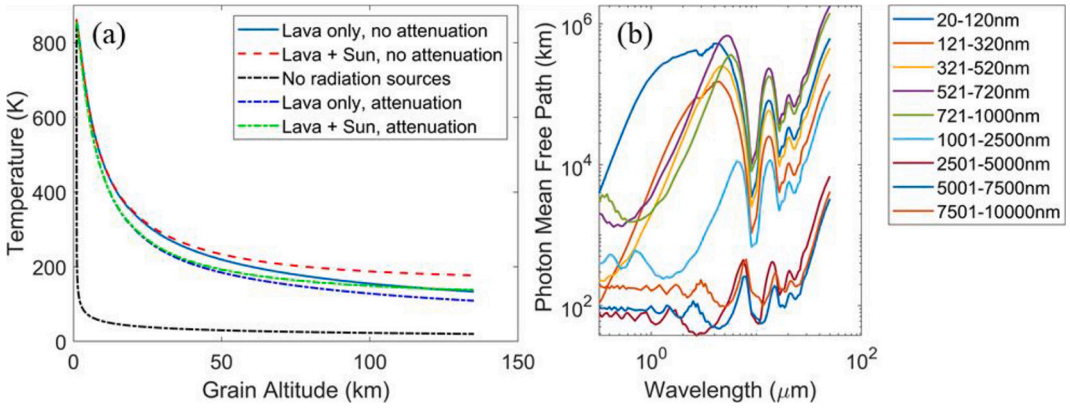

Fig. B.3. (a) Grain temperature as a function of altitude under different radiative transport mechanisms (b) Photon mean free paths for wavelengths between 0.3 and 50 μm relative to different grain classes in the plume. The substantial mean free paths suggest that radiation emitted or scattered by grains within the plume passes through the plume without any interactions.

Appendix C. Details of gas opacity model in PLANET

Our updated opacity model in PLANET improves on the previous version (Zhang et al., 2004), which overestimated the optical depth by relying on the properties of a single central line within a vibrational band at a fixed temperature. The new model calculates spectral absorption coefficients, $\alpha_\nu(T_{SO_2}, n_{SO_2})$, for all lines within each vibrational band, accounting for variations in gas translational temperature (T_{SO_2}) and gas number density (n_{SO_2}). These coefficients are derived from HITRAN data (Gordon et al., 2022) for temperatures ranging from 25 K to 725 K, appropriate for the Tvashtar plume.

From these spectral absorption coefficients, we compute the Planck mean band absorption coefficient, $\overline{\alpha}_i(T_{SO_2}, n_{SO_2})$, for each vibrational band, weighted by the blackbody spectrum $e_{\nu,b}(T_{SO_2})$ within the band's frequency range $\left[\nu_i^l, \nu_i^h\right]$ (see Eq. (C.1)). To reduce computational costs, we pre-compute the Planck mean band cross-sections, $\overline{\sigma}_i(T_{SO_2})$, for each band at temperatures typical of Pele-type plumes and approximate them using polynomial fits to $ln(\overline{\sigma}_i(T_{SO_2}))$, achieving errors below 0.1 % (Fig. C.1). Following Zhang et al. (2003), we use the vent width as the characteristic length scale. If the product of the vent width and $\overline{\alpha}_i$ is less than 1 for a given cell, the cell is considered transparent, allowing emission without immediate absorption. If the product is 1 or greater, the cell is considered opaque, and emission is turned off within that cell.

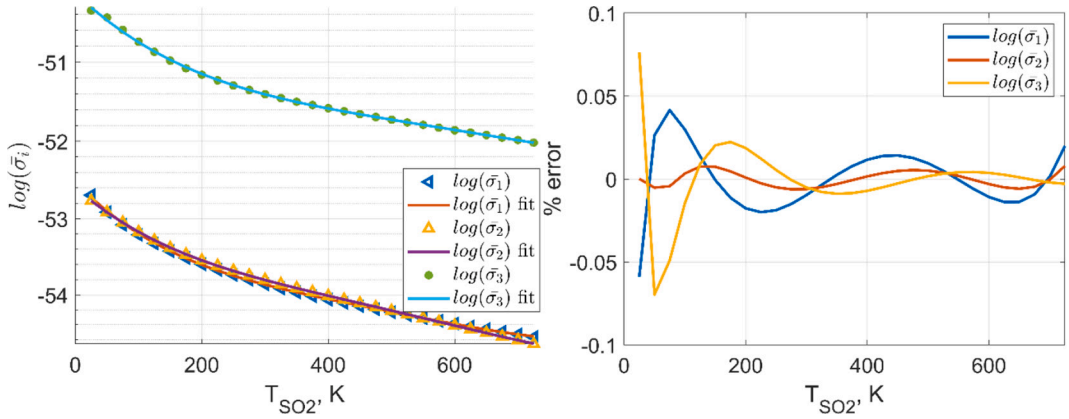

Fig. C.1. (left) Polynomial fit for each Planck mean band absorption cross-section. (right) Percentage error for each fit.

$$\alpha_\nu(T_{SO_2}, n_{SO_2}) = \sigma_\nu(T_{SO_2}) n_{SO_2} \tag{C.1a}$$

$$\overline{\alpha}_i(T_{SO_2}, n_{SO_2}) = \frac{\int_{\nu_i^l}^{\nu_i^h} \sigma_\nu(T_{SO_2}) e_{\nu,b}(T_{SO_2}) d\nu}{\int_{\nu_i^l}^{\nu_i^h} e_{\nu,b}(T_{SO_2}) d\nu} n_{SO_2} = \overline{\sigma}_i(T_{SO_2}) n_{SO_2} \tag{C.1b}$$

This procedure conserves computational time and expense and provides us with a more accurate implementation of the opacity model.

Appendix D. Sensitivity study

Table D.1
Maximum Heights and Widths from Sensitivity Study for Gas Canopy and Grain Class Umbrellas.

	[Umbrella Height, H (km); Umbrella Width, W (km)]									
ṁ [kg/s]	SO_2	20–120 nm	120–320 nm	320–520 nm	520–720 nm	720–1000 nm	1000–2500 nm	2500–5000 nm	5000–7500 nm	7500–10,000 nm
50,000	[273; 601]	[302; 492]	[316; 434]	[316; 365]	[314; 320]	[310; 278]	[294; 199]	[261; 131]	[226; 95]	[199; 74]
66,667	[277; 601]	[300; 507]	[314; 466]	[318; 403]	[316; 359]	[314; 319]	[302; 234]	[277; 158]	[245; 117]	[218; 92]
100,000	**[277; 601]**	**[296; 499]**	**[310; 494]**	**[318; 446]**	**[318; 407]**	**[318; 367]**	**[308; 286]**	**[290; 200]**	**[267; 151]**	**[245; 124]**
150,000	[279; 580]	[294; 483]	[308; 507]	[316; 477]	[318; 444]	[318; 414]	[312; 332]	[302; 248]	[286; 192]	[269; 157]
200,000	[279; 581]	[294; 467]	[302; 503]	[312; 494]	[318; 472]	[318; 442]	[316; 363]	[306; 284]	[294; 224]	[282; 186]
T_0 [K]										
1080	[234; 539]	[247; 420]	[257; 425]	[263; 391]	[263; 358]	[262; 326]	[255; 253]	[242; 181]	[226; 136]	[208; 109]
1180	[255; 565]	[271; 458]	[284; 459]	[290; 415]	[292; 381]	[290; 348]	[281; 268]	[267; 190]	[247; 146]	[228; 117]
1280	**[277; 601]**	**[296; 499]**	**[310; 494]**	**[318; 446]**	**[318; 407]**	**[318; 367]**	**[308; 286]**	**[290; 200]**	**[267; 151]**	**[245; 124]**
1380	[298; 623]	[319; 536]	[339; 526]	[345; 473]	[345; 430]	[343; 387]	[333; 298]	[319; 211]	[288; 158]	[263; 128]
1480	[319; 663]	[343; 571]	[362; 560]	[370; 499]	[372; 451]	[370; 410]	[358; 312]	[339; 221]	[310; 165]	[281; 135]
A [km^2]										
5	[296; 653]	[325; 650]	[343; 666]	[353; 625]	[347; 583]	[347; 542]	[335; 446]	[319; 339]	[306; 264]	[290; 219]
15	[284; 640]	[305; 556]	[323; 560]	[329; 518]	[329; 476]	[327; 433]	[318; 341]	[302; 246]	[284; 187]	[265; 153]
30	**[277; 601]**	**[296; 499]**	**[310; 494]**	**[318; 446]**	**[318; 407]**	**[318; 367]**	**[308; 286]**	**[290; 200]**	**[267; 151]**	**[245; 123]**
45	[273; 577]	[290; 458]	[304; 451]	[312; 405]	[312; 369]	[312; 334]	[302; 257]	[284; 177]	[257; 135]	[234;109]
55	[273; 570]	[288; 444]	[302; 430]	[310; 387]	[310; 351]	[308; 316]	[300; 244]	[281; 167]	[251; 125]	[228;102]
f_g [%]										
0.0	[288; 581]									
2.5	[282; 612]	[300; 498]	[316; 493]	[323; 449]	[323; 412]	[321; 369]	[312; 288]	[296; 204]	[273; 154]	[251; 125]
5.0	**[277; 601]**	**[296; 499]**	**[310; 494]**	**[318; 446]**	**[318; 407]**	**[318; 367]**	**[308; 286]**	**[290; 200]**	**[267; 151]**	**[245; 124]**
7.5	[271; 598]	[290; 497]	[304; 493]	[310; 444]	[310; 402]	[308; 363]	[298; 280]	[282; 198]	[261; 149]	[240; 120]
10.0	[267; 587]	[288; 497]	[302; 486]	[308; 439]	[308; 399]	[306; 359]	[296; 275]	[282; 193]	[257; 146]	[238; 118]

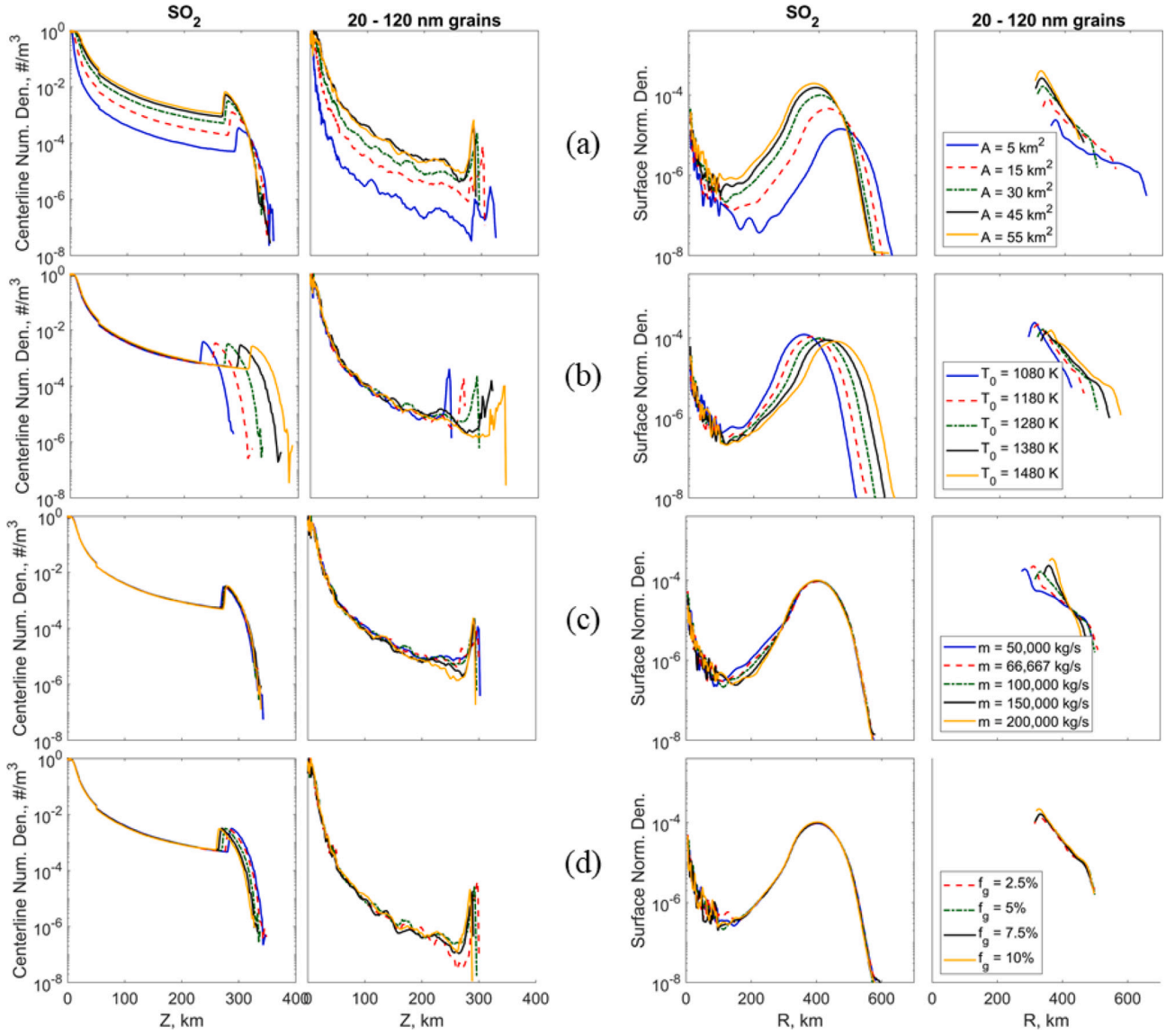

Fig. D.1. Number density profiles for SO_2 gas and 20–120 nm grains (normalized by vent number density) as a function of altitude (left) and radial distance from the vent (right). Investigation of plume structure response to variations in (a) vent area (b) vent stagnation temperature (c) vent mass flow rate (d) grain mass loading.

From Fig. D.1, the heights and widths of the gas shock canopy and the 20–120 nm grain umbrella are recorded in Table D.1. Using plots like in Fig. D.1, other grain size classes respective umbrella heights and widths are also recorded in Table D.1.

D.1. Methodology for calculating elasticity and linear correlation coefficients

We outline a procedure to calculate linear correlation coefficients and elasticities for grain umbrella heights and widths in response to changes in vent parameters, as depicted in Figs. 11 and 12. The linear correlation coefficient assesses the strength and direction of the linear relationship between two variables, while elasticity measures the percentage change in the dependent variable due to a 1 % change in the independent variable. This process is illustrated using the specific example of the relationship between vent stagnation temperature (T_0) and the umbrella height (H) of 121–320 nm grains. The relevant umbrella height data is provided in Table D.1 above.

Table D.2
Logarithmic transformation.

T_0, K	$log_{10}(T_0)$	H, (km)	$log_{10}(H)$
1080	3.0334	257	2.4099
1180	3.0719	284	2.4533
1280	3.1072	310	2.4914
1380	3.1399	339	2.5302
1480	3.1703	362	2.5587

Step 1: Logarithmic transformation of data.
Step 2: Compute $\overline{log_{10}(T_0)}$ and $\overline{log_{10}(H)}$.
Step 3: Calculate the elasticity β, which is the slope of the Eq. (D.1) using Eq. (D.2).

$$log_{10}(H) = \beta log_{10}(T_0) + \alpha \tag{D.1}$$

$$\beta = \frac{\sum \left(log_{10}(T_0)_i - \overline{log_{10}(T_0)}\right)\left(log_{10}(H)_i - \overline{log_{10}(H)}\right)}{\sum \left(log_{10}(T_0)_i - \overline{log_{10}(T_0)}\right)^2} \tag{D.2}$$

In this example, $\beta = 1.0968$, indicating that a 1 % increase in T_0 corresponds to a 1.0968 % increase in H.
Step 4: Calculate the correlation coefficient, r_{height} using Eq. (D.3)

$$r_{height} = \frac{\sum \left(log_{10}(T_0)_i - \overline{log_{10}(T_0)}\right)\left(log_{10}(H)_i - \overline{log_{10}(H)}\right)}{\sqrt{\sum \left(log_{10}(T_0)_i - \overline{log_{10}(T_0)}\right)^2 \sum \left(log_{10}(H)_i - \overline{log_{10}(H)}\right)^2}} \tag{D.3}$$

In this example, $r_{height} = 0.9996$, indicating a very strong/nearly perfect positive linear relationship between T_0 and H.

Appendix E. Fitting plume umbrellas

For each LORRI umbrella, we extract a series of column umbrellas from simulated plume images. After reorienting each umbrella to be centered above Io's North Pole, we draw N lines originating from the North Pole, spanning angles from 0 to 180° relative to the positive *x*-axis. These lines intersect the umbrellas, and the intersection points are recorded. Along each line, we fit polynomials representing the distance from the North Pole as a function of the vent parameters being analyzed (See Fig. E.1). This process generates *N* polynomials, one for each line, which can produce a new umbrella for any set of vent parameters within the range typical for Pele-type plumes. In this study, we consider vent area and stagnation temperature, resulting in third-order two-dimensional polynomials. The *N* polynomial sets are unique to each observation, as they depend on the specific observation geometry of NH, which changes throughout the flyby.

After generating the polynomials, we use them to create an umbrella with specific vent parameters. The umbrella is then transformed back to its original configuration for further analysis (Fig. E.2). Next, we determine the optimal number of lines or polynomials required to accurately represent the umbrellas. To do this, we generate a range of umbrellas with varying numbers of lines or polynomials and compare them with a column umbrella at identical vent parameter values. This comparison involves calculating the root mean square (RMS) of their differences, using Eq. (E.1). In this equation, N represents the number of points in the umbrella, $R_{c,i}$ denotes the distance of the i^{th} point in the column umbrella from the plume's center on Io's limb, and $R_{p,i}$ is the distance of the i^{th} point in the polynomial umbrella. We determined that 200 points provide the best accuracy for the polynomial-generated umbrellas (Fig. E.2). When comparing the difference between the LORRI and polynomial best-fit umbrellas, this RMS is also referred to as the residual root mean square error (RRMSE).

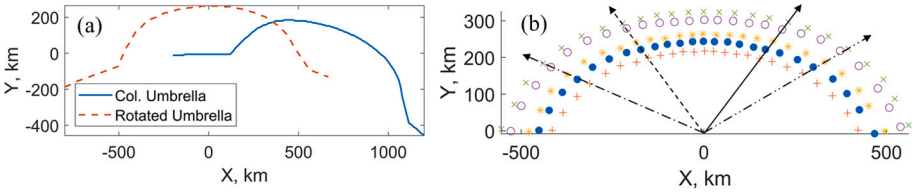

Fig. E.1. (a) DSMC column umbrella (blue solid line) transformed to align with the North Pole (red dashed line). (b) N lines extending from the North Pole at angles from 0 to 180 degrees relative to the positive x-axis. Polynomial fits are applied to the intersection points of the column umbrellas with each line, resulting in a unique polynomial for each line. Each observation corresponds to a distinct set of polynomials. Different marker types are intersection points for various umbrellas, with only 5 umbrellas depicted in this image for clarity. (For interpretation of the references to colour in this figure legend, the reader is referred to the web version of this article.)

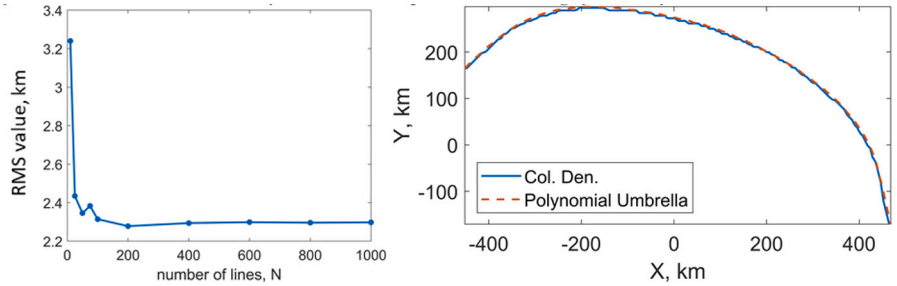

Fig. E.2. (left) Average RMS error of polynomial-generated umbrellas compared to DSMC umbrellas vs. number of lines/polynomials interpolating DSMC umbrellas. (right) Example of a DSMC Umbrella and Polynomial umbrella generated with 200 points.

$$\text{RMS} = \sqrt{\frac{\sum_{i=1}^{N} \left(R_{c,i} - R_{p,i}\right)^2}{N - 1}} \tag{E.1}$$

The accuracy of our Tvashtar plume analysis is limited by various errors introduced at different stages of our method, each with varying magnitudes and significance. These sources of error include DSMC noise, inaccuracies in fitting center coordinates and limb circle radii to Io (see Section 2.5), uncertainties due to plume instability, errors in polynomial fits, and inaccuracies from the Levenberg-Marquardt (LM) least-squares fitting procedure.

The circle-fitting algorithm used to determine Io's limb finds the center and radius coordinates with an accuracy of within 1 pixel for each image. This precision accounts for Io's irregular shape, including bulges and surface features caused by tidal forces. Taking these errors into account, we estimate that our plume umbrella extraction algorithm achieves an accuracy within 1 pixel per data point. This pixel-based uncertainty is then converted to a corresponding length scale for each image, based on Io's actual radius in kilometers. We disregard DSMC noise in this context because our extraction method relies on identifying the outermost cells with non-zero column density values, which results in a simple binary outcome (either zero or non-zero).

To assess the error from polynomial fitting, we generate polynomial umbrellas using the same parameter values as our column umbrellas and calculate the RMS of their differences (as defined in Eq. (E.1)). We average these RMS values across all umbrellas in the parameter space for each observation, yielding the polynomial fitting error. This error is then combined with the circle-fitting error (see Fig. E.3) and provided as input to the LM algorithm.

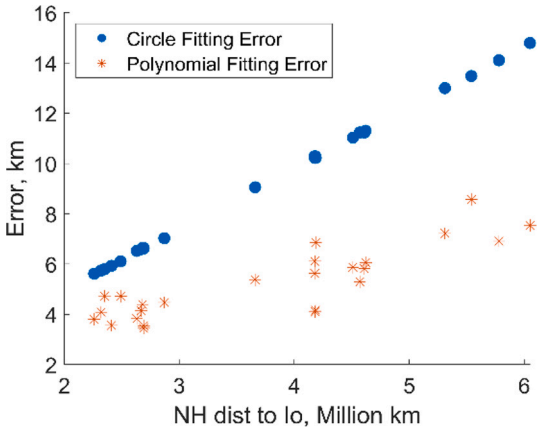

Fig. E.3. 100 LM convergences for a single observation alongside the fitting error associated with each convergence outcome. These data points are aggregated to find the optimal result (average and standard deviation) for each observation.

We establish boundaries on the LORRI umbrella based on two main factors. One boundary defines regions where the umbrella is obscured, such as those in Io's shadow that are invisible to NH or our algorithm. The other boundary is set by areas where we cannot effectively distinguish the plume from residual image artifacts (as seen on the left side of Fig. 13d) after filtering the LORRI images. In cases without these boundaries, the umbrella's limits are determined by its intersection with the limb. We then apply a procedure similar to the one described earlier (Fig. E.1) to the LORRI umbrellas to identify intersection points along lines confined within these boundaries. For these lines, the LM algorithm seeks the set of vent parameters that minimize the function $f(A, T_0)$ in Eq. (E.2), where $R_L, R_p(A, T_0)$ represent the distances of LORRI and polynomial umbrella intersection points from the center of the plume on Io's limb. The terms ϵ_c and ϵ_p represent errors from circle-fitting and polynomial fitting, respectively, while r_1 and r_2 are random values between -1 and 1. The ideal fitting function is Eq. (E.2a), but to account for these sources of observation and fitting process errors, the function provided to the LM algorithm is expressed by Eq. (E.2b).

$$f(A, T_0) = \left(R_p(A, T_0) - R_L\right)^2 \tag{E.2a}$$

$$f(A, T_0) = \left(R_p(A, T_0) - R_L + \epsilon_c r_1 + \epsilon_p r_2\right)^2 \tag{E.2b}$$

The LM algorithm iterates until it reaches 100 convergences, with each iteration aiming to find a local minimum for $f(A, T_0)$. Each run starts with a random initial guess within the domain, and the algorithm refines the estimate with each step. After all iterations are complete, we calculate the final result by averaging the outcomes from the 100 iterations. The standard deviation of these results provides a measure of the uncertainty associated with the least-squares fitting method.

Data availability

Data will be made available on request.

References

Ackley, P.C., Hoey, W.A., Trafton, L.M., Goldstein, D.B., Varghese, P.L., 2021. Hybrid dust-tracking method for modeling Io's Tvashtar volcanic plume. Icarus 359, 114274.

Bird, G.A., 1994. Molecular Gas Dynamics and the Direct Simulation of Gas Flows. Oxford University Press.

Burt, J., Boyd, I., 2004, January. Development of a two-way coupled model for two-phase rarefied flows. In: 42nd AIAA Aerospace Sciences Meeting and Exhibit, p. 1351.

Geissler, P., McEwen, A., Phillips, C., Keszthelyi, L., Spencer, J., 2004. Surface changes on Io during the Galileo mission. Icarus 169 (1), 29–64.

Gordon, I.E., Rothman, L.S., Hargreaves, E.R., Hashemi, R., Karlovets, E.V., Skinner, F. M., Conway, E.K., Hill, C., Kochanov, R.V., Tan, Y., Wcisło, P., 2022. The HITRAN2020 molecular spectroscopic database. J. Quant. Spectrosc. Radiat. Transf. 277, 107949.

Gregg, T.K.P., Sakimoto, S.E.H., Lopes, R.M.C., 2024. Loki Patera, Io: A lava lake masquerade? LPI Contrib. 3040, 2063.

Hoey, W.A., Ackley, P.C., Trafton, L.M., Goldstein, D.B., Varghese, P.L., 2016, November. DSMC simulation of Io's unsteady Tvashtar plume. In: AIP Conference Proceedings, vol. 1786, No. 1. AIP Publishing.

Hoey, W.A., Trafton, L.M., Ackley, P.C., Goldstein, D.B., Varghese, P.L., 2021. Variations in the canopy shock structures of massive extraterrestrial plumes: parametric DSMC simulation of 2007 Tvashtar observations. Icarus 363, 114431.

Howell, J., Siegel, R., 1969. Thermal radiation heat transfer. In: Volume 2-Radiation Exchange between Surfaces and in Enclosures. NASA-SP-164-VOL-2.

Howell, R.R., Spencer, J.R., Goguen, J.D., Marchis, F., Prangé, R., Fusco, T., Blaney, D.L., Veeder, G.J., Rathbun, J.A., Orton, G.S., Grocholski, A.J., 2001. Ground-based observations of volcanism on Io in 1999 and early 2000. J. Geophys. Res. Planet. 106 (E12), 33129–33139.
Jessup, K.L., Spencer, J.R., 2012. Characterizing Io's Pele, Tvashtar and Pillan plumes: lessons learned from Hubble. Icarus 218 (1), 378–405.
Laver, C., de Pater, I., Marchis, F., 2007. Tvashtar awakening detected in April 2006 with OSIRIS at the WM keck observatory. Icarus 191 (2), 749–754.
Mahieux, A., Goldstein, D.B., Varghese, P.L., Trafton, L.M., 2019. Parametric study of water vapor and water ice particle plumes based on DSMC calculations: application to the Enceladus geysers. Icarus 319, 729–744.
Mätzler, C., 2002. MATLAB Functions for Mie Scattering and Absorption, Version 2.
McDoniel, W.J., Goldstein, D.B., Varghese, P.L., Trafton, L.M., 2015. Three-dimensional simulation of gas and dust in Io's Pele plume. Icarus 257, 251–274.
McDoniel, W.J., Goldstein, D.B., Varghese, P.L., Trafton, L.M., 2017. The interaction of Io's plumes and sublimation atmosphere. Icarus 294, 81–97.
McDoniel, W.J., Goldstein, D.B., Varghese, P.L., Trafton, L.M., 2019. Simulation of Io's plumes and Jupiter's plasma torus. Phys. Fluids 31 (7).
McEwen, A.S., Soderblom, L.A., 1983. Two classes of volcanic plumes on Io. Icarus 55 (2), 191–217.
McEwen, A.S., Keszthelyi, L., Geissler, P., Simonelli, D.P., Carr, M.H., Johnson, T.V., Klaasen, K.P., Breneman, H.H., Jones, T.J., Kaufman, J.M., Magee, K.P., 1998. Active volcanism on Io as seen by Galileo SSI. Icarus 135 (1), 181–219.
Milazzo, M.P., Keszthelyi, L.P., Radebaugh, J., Davies, A.G., Turtle, E.P., Geissler, P., Klaasen, K.P., Rathbun, J.A., McEwen, A.S., 2005. Volcanic activity at Tvashtar catena, Io. Icarus 179 (1), 235–251.
Morabito, L.A., Synnott, S.P., Kupferman, P.N., Collins, S.A., 1979. Discovery of currently active extraterrestrial volcanism. Science 204 (4396), 972.
Murray, J.A., Benyahia, S., Metzger, P., Hrenya, C.M., 2012. Continuum representation of a continuous size distribution of particles engaged in rapid granular flow. Phys. Fluids 24 (8).
Pollack, J.B., Toon, O.B., Khare, B.N., 1973. Optical properties of some terrestrial rocks and glasses. Icarus 19 (3), 372–389.
Prem, P., Goldstein, D.B., Varghese, P.L., Trafton, L.M., 2019. Coupled DSMC-Monte Carlo radiative transfer modeling of gas dynamics in a transient impact-generated lunar atmosphere. Icarus 326, 88–104.
Rathbun, J.A., Spencer, J.R., Lopes, R.M., Howell, R.R., 2014. Io's active volcanoes during the new horizons era: insights from new horizons imaging. Icarus 231, 261–272.
Rogic, N., Bilotta, G., Ramsey, M.S., Ferrucci, F., 2019, December. Measured emissivity at very-high temperature and its impact on predicting lava flow run-out distances. In: AGU fall meeting abstracts, 2019. V34C-03.
Smith, M., 2015. MATLAB Central File Exchange. Retrieved from. https://www.mathworks.com/matlabcentral/fileexchange/42904-imoverlay.
Spencer, J.R., Stern, S.A., Cheng, A.F., Weaver, H.A., Reuter, D.C., Retherford, K., Lunsford, A., Moore, J.M., Abramov, O., Lopes, R.M.C., Perry, J.E., 2007. Io volcanism seen by new horizons: a major eruption of the Tvashtar volcano. Science 318 (5848), 240–243.
Trafton, L.M., Poondla, Y.K., Goldstein, D., Varghese, P., 2018, October. Tvashtar's eruption during the flyby of new horizons. In: AAS/Division For Planetary Sciences Meeting Abstracts# 50, 50, pp. 415–416.
Tsang, C.C., Rathbun, J.A., Spencer, J.R., Hesman, B.E., Abramov, O., 2014. Io's hot spots in the near-infrared detected by LEISA during the new horizons flyby. J. Geophys. Res. Planet. 119 (10), 2222–2238.
Zhang, J., 2004. Simulation of Gas Dynamics, Radiation and Particulates in Volcanic Plumes on Io. The University of Texas at Austin.
Zhang, J., Goldstein, D.B., Varghese, P.L., Gimelshein, N.E., Gimelshein, S.F., Levin, D.A., 2003. Simulation of gas dynamics and radiation in volcanic plumes on Io. Icarus 163 (1), 182–197.
Zhang, J., Goldstein, D.B., Varghese, P.L., Trafton, L., Moore, C., Miki, K., 2004. Numerical modeling of Ionian volcanic plumes with entrained particulates. Icarus 172 (2), 479–502.